Postprint of: Leśniewska D., Tordesillas A., Pietrzak M., Zhou S., Nitka M., Structured deformation of granular material in the state of active earth pressure, Computers and Geotechnics, Vol. 157 (2023), 105316, DOI: 10.1016/j.compgeo.2023.105316

Structured deformation of granular material in the state of active earth pressure

Danuta Leśniewska[1], Antoinette Tordesillas[2], Magdalena Pietrzak[3], Shuo Zhou[4] and Michał Nitka[5]

[1]Institute of Hydro-Engineering, Polish Academy of Sciences, Kościerska 7, 80-328 Gdańsk, Poland, corresponding author, e-mail: danuta.lesniewska@ibwpan.gda.pl,

[2]School of Mathematics and Statistics, The University of Melbourne, Melbourne, Australia,

[3]Koszalin University of Technology, Koszalin, Poland,

[4]School of Computing and Information Systems, The University of Melbourne, Melbourne, Australia,

[5]Gdańsk University of Technology, Gdańsk, Poland

keywords: structured deformation, retaining wall, physical state space, displacement state space, local intrinsic dimensionality, digital image correlation

Abstract

The paper focuses on the ability of granular materials to undergo structured deformation by analysing the data from the retaining wall model tests and discrete element simulations. The structured deformation means the movement of a granular material which produces a stable, regular pattern of multiple shear bands. The paper's primary purpose is to study this kind of deformation for the selected data representing the state of active earth pressure of granular materials. The locations of high and negligible shear strains (shear zones and 'dead' zones) in the displacement fields are determined using the shear strains definition. A recently introduced metric called *s*-LID, expressing the perspective of collective grain motion, is applied to the same data. The *s*-LID analysis finds the detailed structure of the localisation pattern directly from displacement data without using the continuum mechanics concept of strains. It is entirely consistent with the digital image correlation analysis in the areas of significant displacement. It expands the knowledge of the deformation structure in small displacement areas, where the digital image correlation method loses its capability. Low *s*-LID and point-like representations in the displacement state space identify nearly rigid zones in the area of high displacements.

1 Introduction

Earth-retaining structures are one of the most important examples of extensive soil-structure interaction. They are recently used in modern transportation systems (Greco, 2013; Xu et al., 2019; Yang & Deng, 2019; Hossein et al., 2022; Hu et al., 2022; Khosravi et al., 2022), ground protection against vibrational and seismic excitations (Ke et al., 2020; Ren et al., 2022), deep excavations (Guan et al., 2022), offshore protection (McGovern et al., 2023), tailing dams (Franks et al., 2021), and other applications. Accurate and realistic assessment of performance and risk of failure of earth retaining structures is an integral part of geotechnical design. The primary role of any retaining structure is the lateral support of the soil or backfill to withstand the imposed horizontal and vertical stresses and ensure overall ground stability. As a result, a vital element in the design of retaining structures is the reliable estimation of the value, distribution and possible evolution of the earth's pressure.

The problem is that the mechanism of the earth pressure still needs to be fully recognized due to the complex, multi-scale nature of the soil response to various loading and environmental factors. Due to it, basic experimental and theoretical research on retaining structures are still being carried out (e.g. Schmüdderich et al., 2020; 2022; Lai et al., 2022; Schweiger & Tschuchnigg, 2021; Hu et al., 2022; Hegde& Murthy, 2022; Khosravi et al., 2016; 2022; Wang et al., 2022; Fathipour et al., 2021). One of the features not accounted for in classical earth pressure theory is *structured deformation*, addressed in this paper. The ability of granular materials to undergo this kind of deformation has already been observed in past X-rays experiments (e.g. James, 1965; James & Bransby, 1971; Milligan, 1974; Milligan, 1983), but to our knowledge, it needs a systematic study.

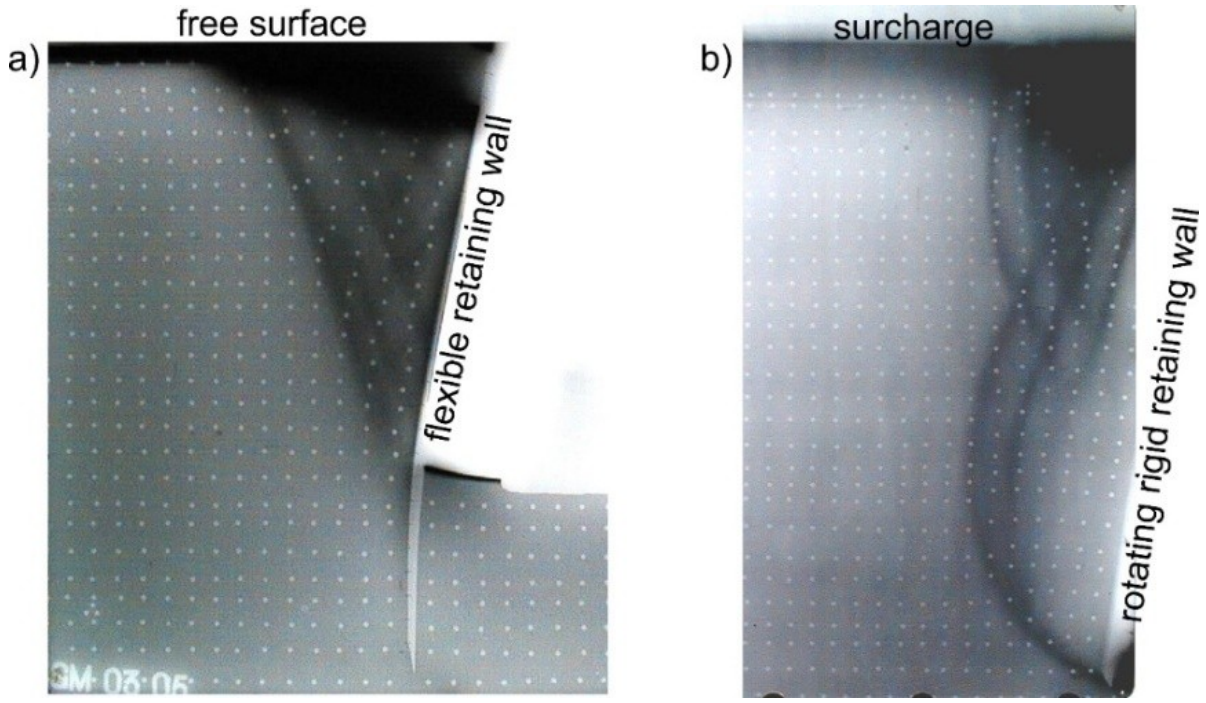

Fig.1. Radiographs made at Cambridge University, showing examples of soil failure patterns (*structured deformation*) behind flexible (a) and rigid (b) model retaining walls. White dots on the radiographs are images of lead shot markers.

We define *structured deformation* as the movement of a granular material producing a stable, regular pattern of multiple shear bands. Fig.1 shows two examples of such phenomenon, recorded by X-rays (Milligan, 1974).

The patterns in Fig.1 correspond to the final stages of the walls' movement in small-scale tests on retaining structures. They are visible due to the reduction of the granular material density caused by dilation, characteristic of shear bands. Multiple shear bands in Fig.1a (excavation of a flexible wall) and Fig.1b (rigid wall rotating about its toe in out of soil direction) form a regular network, including characteristic rhomboidal elements created by intersecting bands (Leśniewska, 2001). The bands also appear in traditionally considered rigid areas (e.g. soil wedge behind the flexible wall in Fig.1a, usually referred to as the Coulomb wedge, Coulomb, 1776).

Leśniewska and Mróz (2000) noticed the issue of regular shear bands in granular materials and proposed an analytical explanation of the most simple discrete pattern consisting of parallel straight shear bands. Introducing the elastic wall parameter into classic Coulomb wedge analysis was the solution in this case; however, such a simple approach becomes inefficient in explaining more complex patterns, like the ones in Fig.1.

The traces of structured deformation also exist in some finite element solutions of a retaining wall problem or DEM simulations. However, they are often treated with some suspicion as potential numerical artefacts. An example of such a shear band pattern is shown in the paper by Loukidis and Salgado, 2013. They found the developed discrete patterns of shear strains resembling the real ones and noticed the change of the earth pressure distribution from smooth to developing peaks and valleys. They concluded that it is a consequence of the shear banding inside the sliding mass. It confirms our assumption that understanding the earth pressure development behind a retaining wall requires studying the structured deformation; however, the direct quantitative relation between structured deformation and the earth pressure evolution appears challenging to establish at this research stage.

Based on Fig. 1, we assume that the structured deformation on a macro scale appears as ordered, alternating areas of intense and negligible shear strains resulting from the different local organisation of grain displacements. Such an internal division of motion should be detectable not only by the material density changes, like in the case of X-rays, but also in the displacement field, provided that an appropriate tool is employed to analyse the collective movement of many data points. A recently introduced metric called *s*-LID, already applied by Tordesillas et al. (2022) to demonstrate the structural deformation of a granular sample in the elemental biaxial test, was selected.

It is a promising tool for analysing more complex deformation mechanisms characteristic of boundary value problems, an example of which is the retaining structure. *s*-LID is a metric based on the *Local Intrinsic Dimensionality* (LID) concept initially proposed by Houle (2017). In essence, *s*-LID accesses the intrinsic dimensionality of a reference point to its *s* nearest neighbours (*s*NN). That is the minimal number of latent factors required to represent a given neighbourhood. It can serve as a quantitative measure of how outlying a grain's motion is (depending on the *s*-LID score) to capture regions with abnormal or negligible motions.

Our paper uses the *s*-LID method to investigate the deformation structure of granular material in the state of active pressure. Two characteristic displacement fields, one coming from the experimental model test and the other simulated by the discrete element method (DEM), are analysed to achieve this goal. The test and DEM simulation are described in detail by Leśniewska and Muir Wood, 2009, 2010; Muir Wood and Leśniewska, 2011 and Leśniewska et al., 2020. Since the *s*-LID method has not been widely used for soil mechanics problems, some initial verification with the commonly accepted tools is recommended. That is why the *s*-LID analysis is preceded by a preliminary one, performed on the selected displacement fields, using corresponding shear and volumetric strains, calculated with DaVis8 discrete image correlation (DIC) software. The purpose of this preliminary analysis is a simplified recognition of the selected elements of the deformation structure, facilitating the interpretation and verification of a complete structure obtained later in the paper using the *s*-LID method.

The DIC (or PIV) method of calculating strains from displacement fields has become a fundamental tool in the experimental analysis of granular materials. It is a non-destructive optical method to determine granular material displacements, where grains serve as tracers.

High-resolution deformation monitoring can be achieved by processing successive digital images (Rechenmacher & Finno, 2004; Słominski et al., 2007; Stanier et al., 2016; White et al., 2003, 2005).

The paper is arranged as follows. Section 2 discusses the displacement data sources – the model test on a retaining wall and its discrete element (DEM) simulation. Section 3 presents the selected displacement fields and their characteristics in 2D physical state space (PSS) and displacement state space (DSS). In PSS, the measurement points (e.g. grains) are described by their x and y coordinates and in DSS, by horizontal and vertical displacements v_x and v_y (a scatter plot). Section 4 discusses the results of the preliminary analysis of the selected displacement fields. In Section 5, the *s*-LID method is introduced, and the results of the final analysis of the displacement fields are given and compared to standard DIC analysis results. The conclusions are summarized in Section 6.

2 Sources and types of the selected displacement data

2.1. The type of test being analysed

We use the numerical and experimental displacement fields taken from the small-scale **P-3D** model test (test number 070528 in our database) and its simulation, discussed in detail by Leśniewska et al. (2020). P-3D testing involves relatively large granular samples placed in rectangular boxes of finite depth, which is significantly smaller than the other two dimensions (see the sketch in Fig.2a). Small (compared to the depth of the test box) 3D grains are usually used, and any external loading is uniformly distributed along the (z) dimension. Such tests are called pseudo-3D because, despite their actual 3D geometry, they create plane strain conditions on a macro scale - deformation of a granular sample along its depth (z) is negligible compared to deformation in the other two directions (x, y plane).

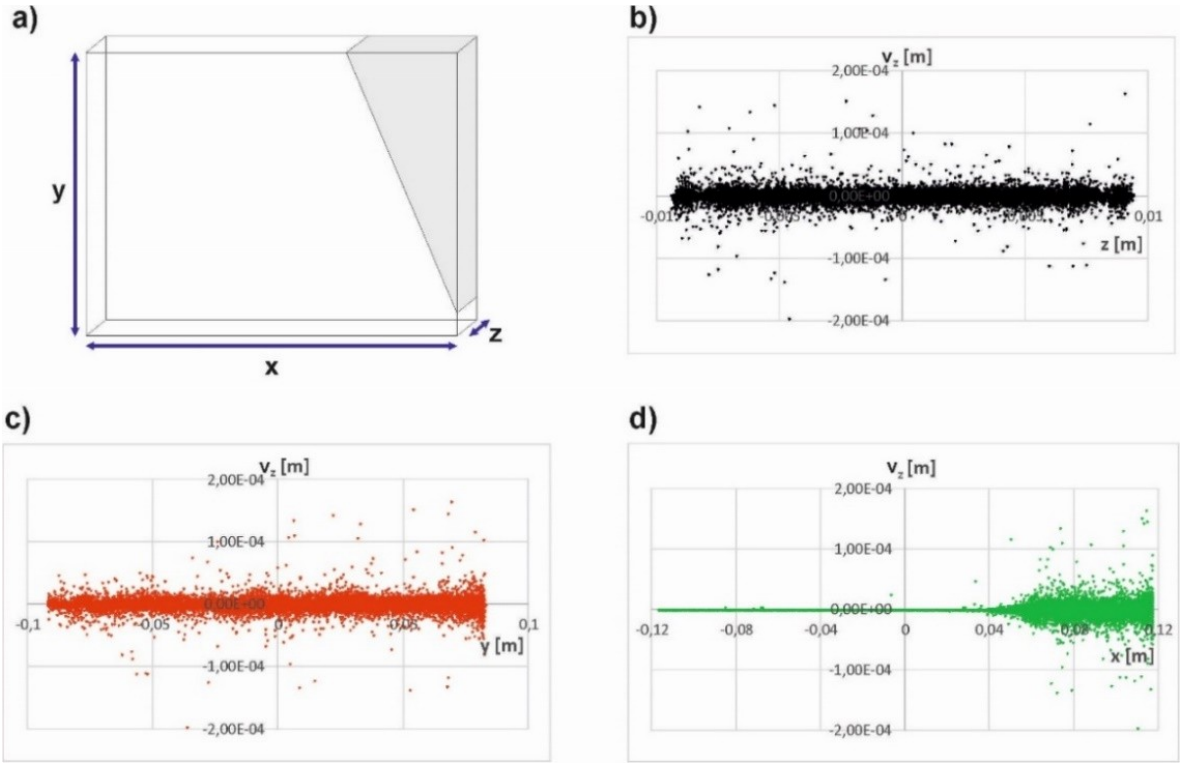

Fig.2. The out-of-plane grain displacement v_z in 3D DEM simulation of a P-3D test. a) schematic geometry of a sample in a P-3D test, b), c), d) – v_z as a function of z, y and x.

However, in the micro-scale, some out-of-plane grain movements are possible because the sample consists of more than one non-flat 'layers', and grains have a chance to rearrange also in (z) direction. Fig.2 illustrates this effect - it contains the results of a 3D DEM simulation of the test with the same geometry as the test 070528 (Fig.2a), using about 100 000 grains, two times larger than in the actual test.

Fig.2b-d shows that some grains show non-zero displacements in the out-of-plane direction, which are a function of x, y and z: they are evenly distributed over the entire depth of the sample (Fig.2b), show the increasing scatter with its height (Fig.2c) and appear only in the deformation wedge typical for retaining structures (Fig.2d), schematically marked in grey in Fig.2a. It is worthy of note that the maximum displacement v_z is about 0.2 mm, i.e. about 10% of the D_{50} grain diameter, equal to 2.0mm.

The existence of the out-of-plane grain motion, confirmed by 3D DEM, makes it difficult to directly compare some of the experimental and simulated results. The reason is that the 2D images recorded during the experiment are made in transmitted light, thus representing a superposition of information from different layers of the sample (they are 'averaged' over the depth). It is possible because transparent grains were used. Multiple ‘layers’ also allow for some competing failure mechanisms to be created in the sample at different test stages - the predominant mechanism is only established in the final stage at significant wall displacements. The simplest failure mechanisms can also be observed at the initial test stages. Examples of the competing failure mechanisms behind a rigid retaining model wall can be found, for example, in Leśniewska and Muir Wood, 2011 (Fig.19). It is difficult and time-consuming to create similar ‘transmission’ images based on 3D DEM results. The other solution, accepted in this paper, is to use the corresponding 2D simulations, bearing in mind that it cannot reproduce any out-of-plane grain movements.

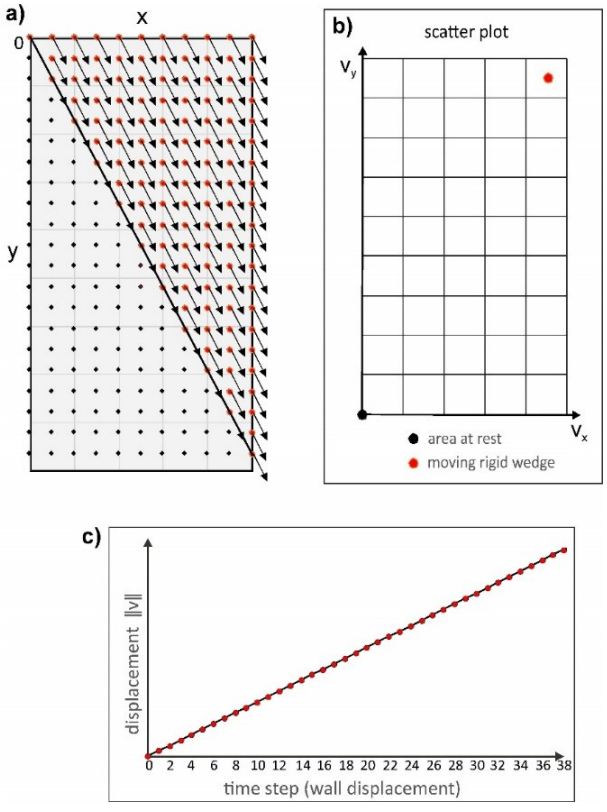

Fig.3. Idealized case - a rigid wedge sliding on an inclined plane: a) discretized displacement field, b) scatter plot, c) evolution of the wedge displacement as a function of the number of wall displacement increments (time steps).

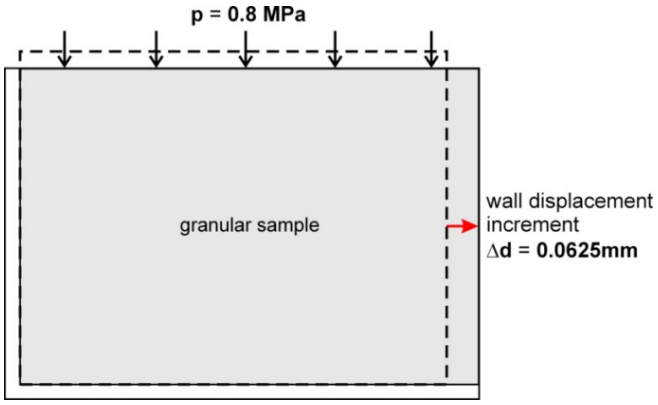

Fig.4. The layout of the retaining wall model test and its boundary conditions: the incremental horizontal translation of the right boundary and constant external loading of the top boundary (through five adjusting rigid blocks, Leśniewska et al., 2020).

2.2. Idealised case - rigid wedge sliding on an inclined plane

The following part of the paper will discuss the representation of the displacement field behind a retaining wall in the physical space (PSS) and kinematical displacement space (DSS). We start from the idealised case of a rigid wedge motion along an inclined plane, corresponding to the classic Coulomb approach (Fig.2a).

A limitation on the wedge displacement rate is assumed to agree with the test scheme (Fig.4). Fig.3a shows the example of discretised displacement field that can represent this type of motion in the PSS - displacements of constant value and direction only inside the wedge. Therefore, this field, presented in DSS (as a scatter plot, Fig.3b), consists of two points only: the first at the beginning of the coordinate system, representing all points with zero displacements outside the wedge, and the second (red circle) corresponding to all points of constant displacement inside the wedge.

The position of the red point on the scatter plot depends on the value and direction of the wedge displacement. The fact that points belonging to a particular rigid area form one point in a scatter plot helps to interpret more complex displacement fields later in this paper.

The other observation, helpful in studying more complex kinematics, is that for any rigid body motion and the corresponding discretized displacement field, the displacement of any focal point (central for a given neighbourhood) selected in this field must be equal to the average displacement in its vicinity:

$$d_k = d_{N-av} \quad , \qquad (1)$$

where d_k is the total displacement of a focal measuring point after k time steps, and $d_{N\text{-}av}$ is the corresponding mean displacement of the neighbourhood consisting of N measuring points.

Therefore, Eq.(1) is fulfilled in any area experiencing rigid body motion. This area can be found by simply calculating the mean displacement in a particular neighbourhood and comparing it with the focal grain displacement. If both are equal or very close, the neighbourhood moves as rigid or close to a rigid body. If the evolution of the wedge displacement in time is considered, the total wedge displacement increases linearly with the displacement of the wall, as shown in Fig.3c.

2.3. Experimental model test

Fig.4 shows the test layout and its stress and displacement boundary conditions. The dimensions of the granular sample were 23.5x18.5x2.0cm, with the total number of grains in a range of 10^6. Full-field displacements were obtained using standard digital photography and 2D image analysis by digital image correlation (DIC). Horizontal translation of the model wall was applied in 0.0625mm increments (to be compared with D_{50} grain diameter equal to

1.0mm) at constant external stress 0.8MPa. The final cumulative wall displacement reached about 3.5mm. The wall movement was independent of the sample. The test is described in detail by Leśniewska et al. (2020).

Table 1: Material constants used in DEM simulations

E_c [GPa]	ν_c [-]	μ [°]	β [-]	η [-]	R [m]	ρ [kg/m^3]	α [-]
2.4	0.3	20	0.3	0.005	0.001	2550	0.08

2.4. Numerical model test

The so-called soft-particles approach was employed to simulate the experimental test, allowing the particles to overlap to account for their deformation (Frost et al., 2002; Gu et al., 2017, Luding, S., 2004; Nitka &Grabowski, 2021; Salazar et al., 2015; Zhao et al., 2018). The computations were performed using the open-source 3D numerical code YADE (Kozicki & Donze, 2008; Chèvremont et al., 2020; Hartmann et al., 2022; Kozicki et al., 2022; Maurin, 2018; Thoeni et al., 2014; Thoeni, 2021). Calculations by YADE consisted of two steps: (1) computing the interaction forces between elements (grains) in contact and (2) computing the resulting acceleration of each element (grain) using Newton's second law of mechanics. The time integration of its acceleration gave the new position of the element (grain).

DEM model, including rolling resistance, proposed by Kozicki and Donze (2008), was accepted in simulations, characterized by five main local material parameters: E_c (the modulus of elasticity of grain contact), ν_c (Poisson ratio of the grain contact), μ (the inter-particle friction angle), β (coefficient of rolling stiffness) and η (the rolling coefficient). Besides, the particle radius R, the particle density ρ and the numerical damping parameter α are required. The detailed model's equations are given in Leśniewska et al. (2020). Table 1 contains the material constants accepted in the simulation. They were found based on

numerical, three-dimensional (3D) triaxial compression tests with rigid walls on a 10× 10×10cm^3 sample of small spheres. Numerical results have been verified by the actual triaxial compression data published by Cui et al. (2017). The entire calibration process is reported by Leśniewska et al. (2020).

The rolling coefficient ï resulting from the calibration procedure, is extremely low ($\eta = 0.005$) compared to that of sand particles ($\eta = 0.4$, Nitka & Grabowski, 2021) – it is justified by the round, but not ideally spherical shape of the glass beads. The effect of the damping parameter, if $\alpha \leq 0.08$, was insignificant in quasi-static calculations (Kozicki et al., 2013).

Only a single layer of grains was modelled to facilitate finding the potential deformation structure and to spare the calculation time. As a result, a single-layer sample was created, consisting of 45 300 grains.

The boundary conditions adopted in the numerical simulations are consistent with Fig.4: the incremental horizontal translation of the right boundary (0.0625mm displacement increment) and the constant external load (0.8MPa) applied to the top boundary through five adjacent rigid blocks. Simulations started with setting the external load and were continued by applying horizontal translation to the vertical wall, thus imposing the active earth pressure state. The wall translation rate was low enough to ensure the quasi-static conditions.

2.5. The basis for the selection of displacement fields

The two examples of displacement fields were selected for the analysis, one experimental and the other simulated, corresponding to the wall displacement of 0.313mm and 2.375mm, respectively (Fig.5). The basis for their selection is a similar simple failure mechanism, not the same wall displacement.

Such a mechanism consists of a dominant shear band (Fig.5c, d), cutting off a triangular wedge in the displacement field (Fig.5a, b). It can be observed mainly in the initial phase of the experiment, where no competing failure mechanisms appear, as mentioned in Section 2.1.

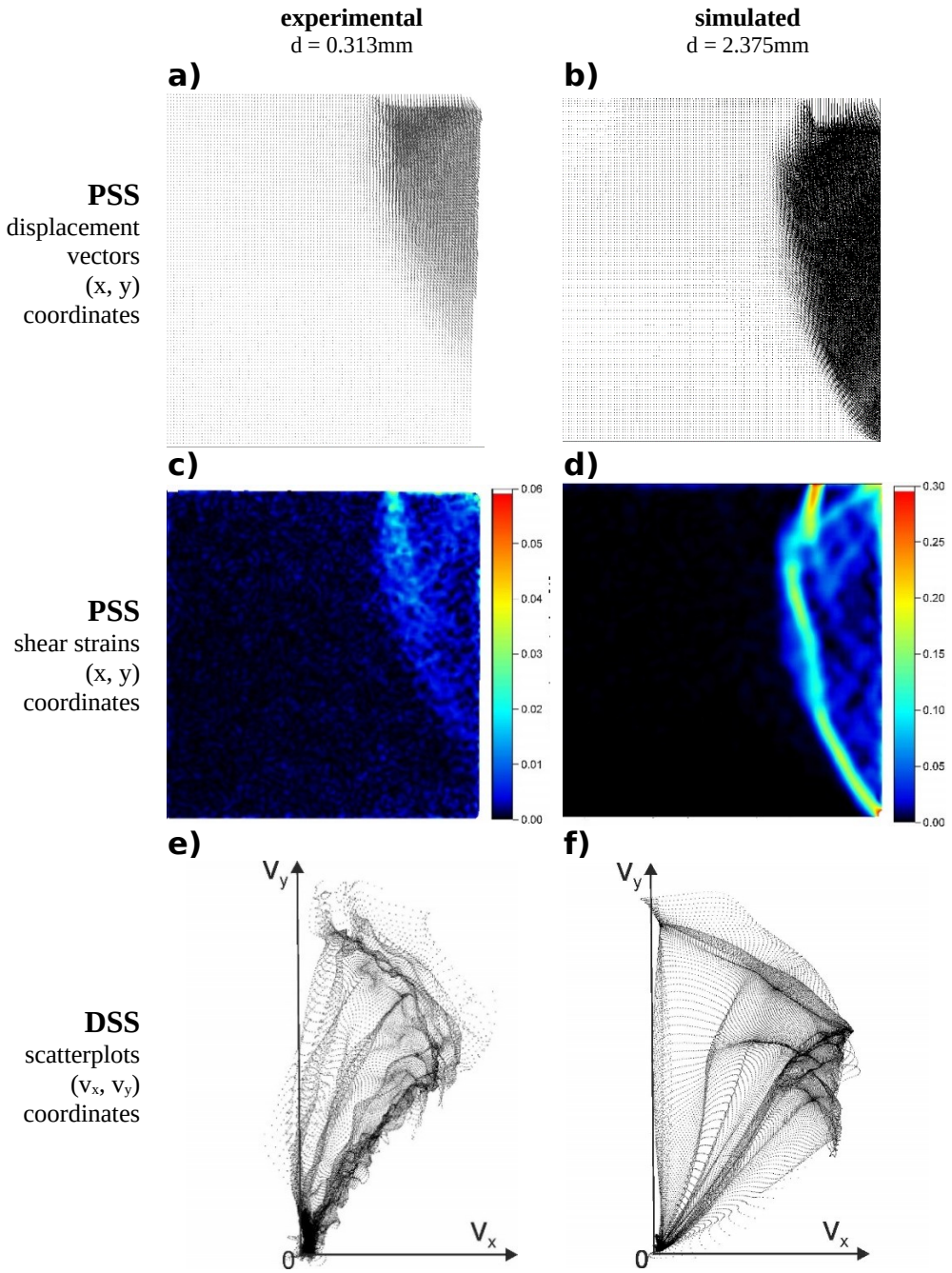

Fig.5. Displacement data, representing the initial stage of the experiment (left column) and the final stage of the DEM simulation (right column): **(a)**, **(b)** - displacement vectors, **(c)**, **(d)** - the corresponding shear strain maps (PSS), **(e)**, **(f)** - displacement fields (a) and (b) as scatter plots (DSS).

The experimental verification of the DEM simulation was already done by Leśniewska et al. (2020). The present paper aims to investigate the specific structures in the displacement fields behind a retaining wall. It will be demonstrated in the proceeding sections that the 2D simulation more clearly shows this structure; therefore, it was chosen as the primary data source to apply the *s*-LID analysis.

The experimental displacement field was only added to show that the deformation structure revealed in the simulations is not just a numerical artefact but can also be found in actual data, albeit less clearly.

3 Representation of the selected displacement fields in PSS and DSS space

The displacement fields analysed in this paper were obtained by image analysis (DIC method). The experimental images of size 2560x1920 pixels were acquired using Sony Digital Still Camera DSCF717. The distance of 1mm, representing D_{50} grain diameter, corresponds to about 12 pixels in these images. The images of the DEM simulation are screenshots of size 1920x1080 pixels.

Displacement vector fields were calculated using a patch size of 41x41 pixels, with a step size of 4 pixels for the experimental test and 2 pixels for the DEM simulation. It created about 21000 and 35000 displacement measurement points in sub-grain resolution corresponding to about 6 measuring points per grain in the experimental and about 12 in the simulated displacement field.

Figs 5a and b show the two selected examples of displacement fields. Figs 5c, d contain the corresponding shear strain maps, calculated by DIC, where the high and low deformation areas are colour-coded (red and yellow - high, blue and dark blue - low). Both maps show the

strong localization of shear strains, cutting off some Coulomb-like curvilinear wedges. Inside the wedge, in contrast to the classic image of the Coulomb wedge as a rigid body, weaker ('micro') bands are visible, indicating that the interior of the wedge is undergoing some deformation.

The image of the primary shear band is more apparent in the case of DEM simulation (Fig.5d). Some ordering of the micro-shear bands inside the wedge can be seen, not observed in Fig.5c.

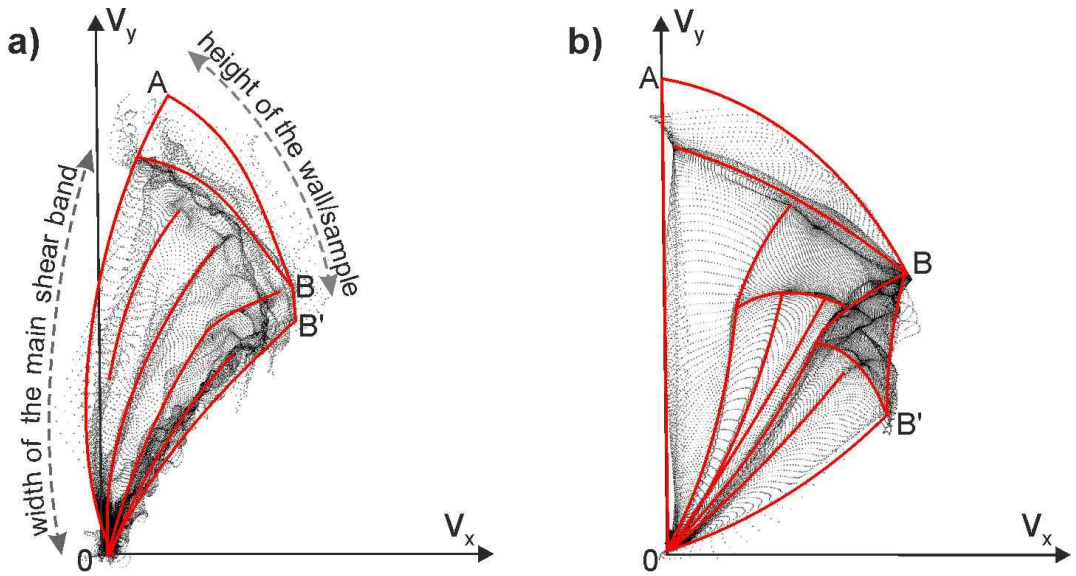

Fig.6. Approximate division of the scatter plots, representing: **a)** the initial stage of the experiment (Fig.5e), **b)** the final stage of the DEM simulation (Fig.5f).

Figs 5a and b are a standard presentation of the displacement field in physical-state space PSS. Figs 5e, f show the same data as scatter plots, where v_x and v_y are displacement components in x and y direction.

Fig.6a shows that most of the scatter plot points in the case of the retaining wall test fill the interior of a particular curvilinear triangle OAB, with one of its vertices at the origin of the coordinate system. The triangle is subdivided by radial lines originating at point O and defining the regular structure of the displacement field. The existence of the structure is

difficult to guess when looking at Fig.5a. Similar structure is present in the simulation (Figs 5f and 6b); however, in this case, the lines of the scatter plot's divisions are much more smooth. The most obvious difference is the area OBB', well developed and containing much detail in Fig.6b and reduced and devoid of precise details in Fig.6a. The reason for more randomness in the case of the experimental data is probably the earlier mentioned fact that the simulation is made for one layer of grains only. The experimental sample consists of some 20 layers, giving the grains additional degrees of freedom in an out-of-plane direction. Some physical explanations for the divisions shown in Figs 5e, f and 6 will be given later in the paper.

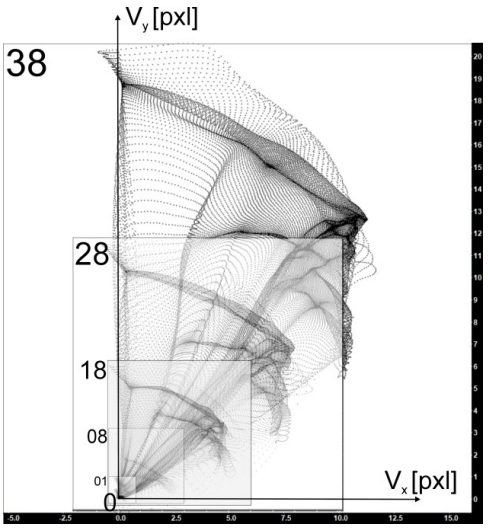

Fig.7. Scatter plots of displacements after steps 01, 08, 18, 28 and 38 of the DEM simulation.

Despite the apparent differences between Fig.5e and 5f, both scatter plots have enough common features to be analysed in the same way. Therefore, in the next chapter, the significance of individual elements of the scatter plot structure and its evolution over time will be investigated.

4 Characteristics of scatter plots for a retaining wall problem

4.1. DEM simulation – preliminary analysis of the displacement field

DEM simulation of the translating retaining wall (Fig.4) consisted of 38 wall displacement steps of 0.0625mm and reached the total wall displacement d = 2.375mm. Fig.7 represents the evolution of the displacement's scatter plot during the whole course of the simulation. Each step's scatter plot consists of about 300 000 points, so for picture clarity, only 5 displacement steps are shown (01, 08, 18, 28 and 38).

Fig.7 shows that the visible structure of scatter plots does not change significantly during the simulation, and the increase in the total wall displacement only causes its expansion. It is assumed that any observations concerning the structure of displacement fields described in the following chapters are valid regardless of the considered time step.

The above finding also applies to the experiment, provided that the stages corresponding to a single failure mechanism are considered separately (as noted in Section 2.1, in the case of a multi-layer sample in P-3D tests, some competing failure mechanisms may coincide, complicating the displacement field).

Fig.1 suggests that two types of elements may constitute the deformation structure: shear bands (dark zones), where the granular material deforms extensively, as evidenced by changes in the position of the lead shot markers (white dots), initially located in the nodes of the square-meshed net, and areas of low deformation (approximately retaining the initial marker pattern) closed between the intersecting shear bands. Such zones are referred to by Tordesillas et al., 2022 as shear zones (SZ) and dead zones (DZ), respectively. This study aims to confirm the coexistence of these two types of zones in the displacement field behind the retaining wall and to characterize their kinematics using the *s*-LID analysis described in Section 5. In order to correctly interpret the future *s*-LID results, firstly location and kinematics of the selected

fragments of SZ and DZ zones in the PSS and DSS will be determined directly from the definition of shear strains in 2D:

$$\varepsilon_{xy}=\frac{1}{2}\left(\frac{\partial v_y}{\partial x}+\frac{\partial v_x}{\partial y}\right) \quad , \quad (2)$$

where v_x and v_y denote displacement components in x and y directions.

Fig.5d shows a typical 2D shear strain map for a retaining wall. This map will explain the origins of the division lines in Fig.5f (the same lines are marked red in Fig.6b). We will also demonstrate which separated areas or lines may correspond to SZ or DZ. For this purpose, the shear band in Fig.5d was divided into equal squares with a dimension corresponding to the approximate width of the shear band, estimated from the strain map assuming a shear strain value greater than 10%, which corresponds to the light blue colour in Fig.5d.

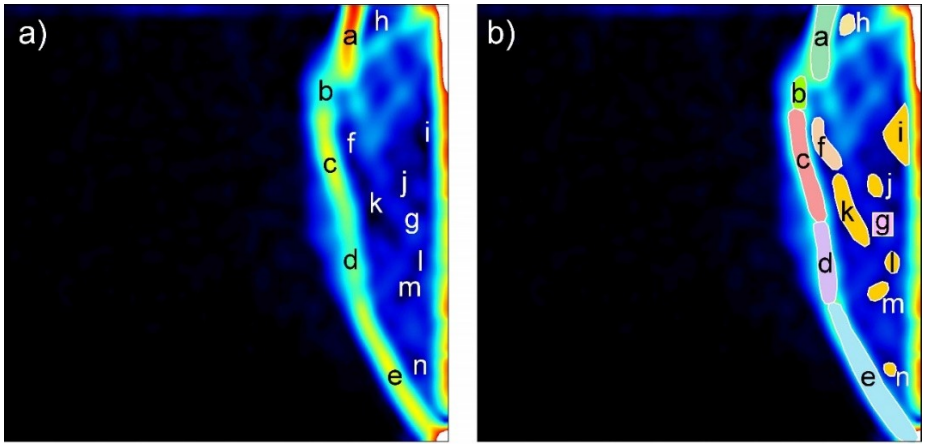

Fig.8. Areas of different shear strain values selected for data interpretation in DSS: **a)** – the approximate location on the shear strain map, **b)** – extension and colour code.

Next, the shear strain and displacement data were double-filtered in the following way:

- first, several characteristic regions with high or low strain values have been identified from the shear strain map (Fig.8a),
- second, the ranges of shear strain values for these areas and the corresponding ranges of coordinates (x, y) of the measurement points belonging to them were read from the DIC numerical files,

- third, the (x, y) coordinates were used as filters on the original displacement data to split them into subsets related to the selected ranges of shear strains,
- finally, the original and filtered displacements were plotted together as a scatter plot.

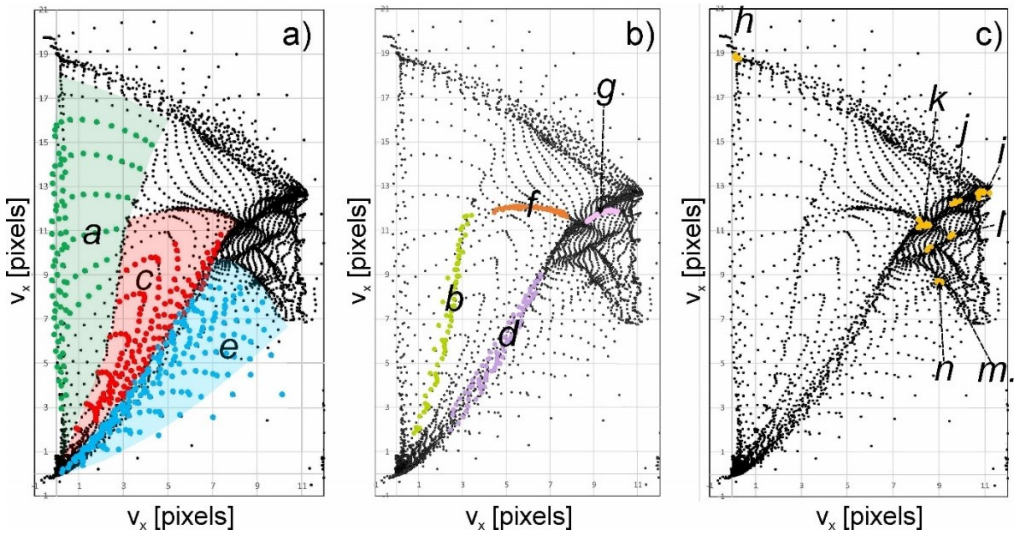

Fig.9. Scatter plots with the reduced number of points showing locations corresponding to the areas from Fig.8b in DSS space.

The regions ('samples') in Fig.8 belong to the primary shear band (**a**-**e**) or lay inside the curvilinear wedge delimited by it (**f**-**n**). The shear band seems non-uniform in terms of the shear strains – the areas **a**, **c** and **e** present visibly higher strains than **b** and **d**. Shear strains in the areas **h**-**m**, marked yellow in Fig.8b, are the lowest and can be regarded as parts of potential DZ, while the areas **f** and **g** represent the intermediate strains.

The following approximate ranges of shear strains were filtered out: 0.12 - 0.18 for the areas **a**, **c** and **e**, 0.09-0.12 for **b** and **d** and 0.002-0.007 for **h**-**m**. Fig.9 presents the results of the double filtering procedure as scatter plots using the colour code from Fig.8b. For clarity, only every sixteenth point of the complete data set from Fig.5f is shown.

Fig.9a confirms that the shear zone, commonly considered a single shear band, consists of three kinematically distinguished segments: **a**, **c**, and **e**, physically separated in the PSS space and adjacent in the DSS space. The material in these segments can move in different

directions but within limits defined by the opening of each part of the scatter plot 'fan'. This opening and the distances between measurement dots in **a**, **c**, and **e** mean that grains from close neighbourhoods move in different directions with different displacement rates, as commonly expected of SZ. As shown in Fig.6, going from segment **a** in Fig.9a, through **c** to **e**, we move from the top to the bottom of the strain localisation, i.e. from the top to the bottom of the analysed retaining structure. Moving up from the point (0,0) of segment **a** (for example), we cross the shear band from left to right.

The area of the scatter plot covered in Fig.9a by **a**, **c** and **e** confirm the common knowledge that it is in the strain localization that the most significant changes in the kinematics of the granular material occur.

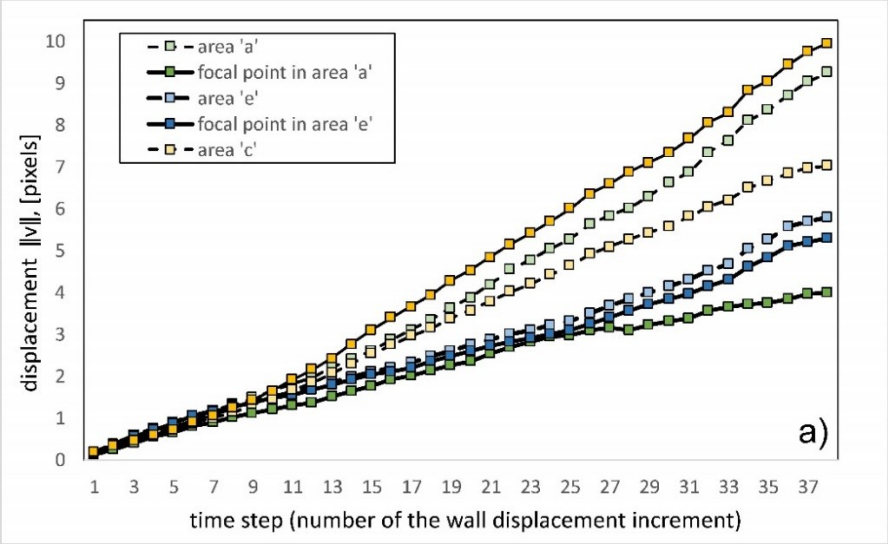

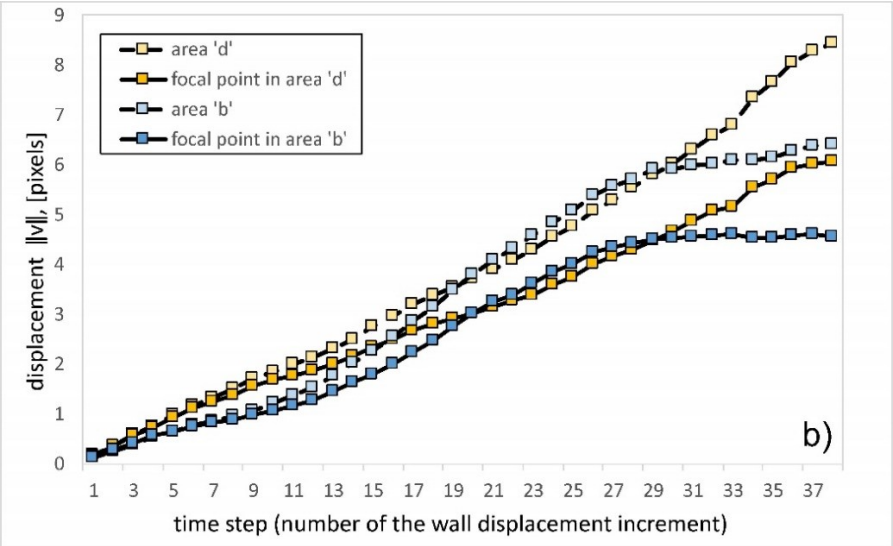

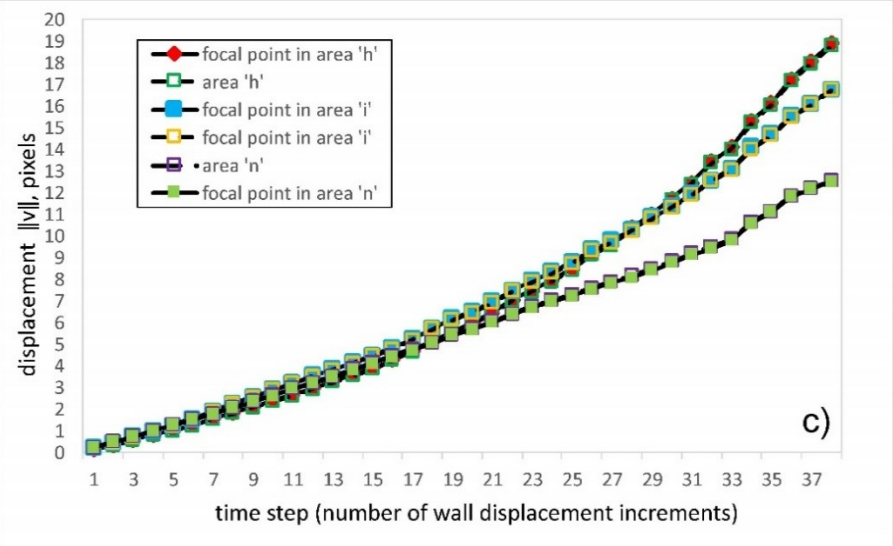

Fig.10. Displacement value evolution for the selected focal points compared to their closest neighbourhood's average displacement in the areas: **a)** *a*, *e* and *c*, **b)** *b* and *d*, **c)** *h*, *i* and *n* (Fig.8b).

Fig.9b shows the displacement distributions in areas **b** and **d** – interestingly, they form borderlines between areas **a**-**c** and **c**-**e** from Fig.9a, respectively. Their linearity suggests some additional constraints imposed on grains' motion, compared to **a**, **c** and **e** – the grains there move approximately in one direction, however, by different displacements. Similar linear distributions characterize areas **f** and **g**. The rest of the selected regions (**h**-**m**) show another worth to note feature in DSS (Fig.9c) – each contains from a dozen to several dozen measurement points; however, in the scatter plot, they are very close to each other. Such concentration represents close to rigid motion (Section 2.2), so the existence of DZ in the

displacement field is confirmed. Each selected quasi-rigid area has its specific displacement vector (a different position on the scatter plot), meaning they are kinematically independent. The question is whether they are permanent or temporary. Several focal points were selected to check it, representing regions **a**-**n** (Fig.8) and their closest neighbourhoods, covering about 20 measurement points.

Fig.10 compares the changes in the displacement of individual focal points with the mean of the immediate neighbourhood as a function of time steps. Starting from the areas **a**, **c** and **e** (Fig.10a), the clear difference between d_k and $d_{N\text{-}av}$ (Eq.(1)) appears around the 9th time step and is growing quasi-linearly. It is the largest in **a** (light and dark green markers) and the slightest, but detectable in **e** (yellow and orange). In the case of DZ (Fig.10c), preselected in Fig.9c, d_k and $d_{N\text{-}av}$ almost perfectly coincide from the first to the last time step, confirming their motion is permanently close to that of a rigid body.

The evolution of d_k and $d_{N\text{-}av}$ in the areas **b** and **d** (Fig.10b) at the final stage of simulation seems to reach the state of constant displacement; however, with different values – this suggests a way of movement that is difficult to classify as SZ or DZ, what Fig.11 best illustrates.

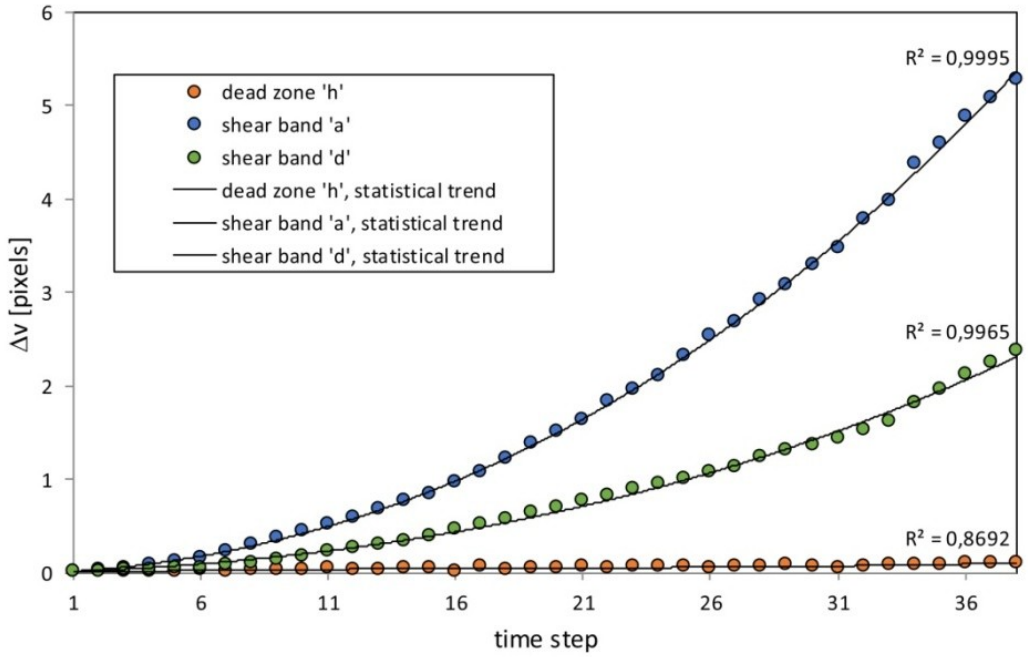

Fig.11. The statistical trend of the difference between the selected focal points' displacements and the average displacement of their neighbourhoods, in areas **a**, **d** and **h** in Fig.8b.

This figure shows the statistical trend of the absolute difference °v between displacements of the selected focal points and the average displacement of their immediate neighbourhood, as a function of the time step, for the data from Fig.10.

In the area **h** (orange circles), °v takes a value close to zero from the beginning to the end of the simulation, confirming that it is subject to permanent close-to-rigid motion, expected for DZ. In contrast, in the area of **a** (blue circles), it grows significantly, which proves the decreasing coordination of grain movement, characteristic of SZ. The °v plot for area **d** (green circles) suggests a way of movement of the granular material inconsistent with neither DZ nor SZ. Looking at Fig. 9b, it becomes clear that the material motion in region **d** is represented in the scatter plot by some well-defined curve, not an extensive 2D area or neighbourhood of a point as in the case of **a** or **h**. The linearity of the area **d** in the scatter plot suggests grain movement approximately in one direction; however, not with constant velocity (like in a laminar flow), less constrained than in DZ, but not as free as in SZ.

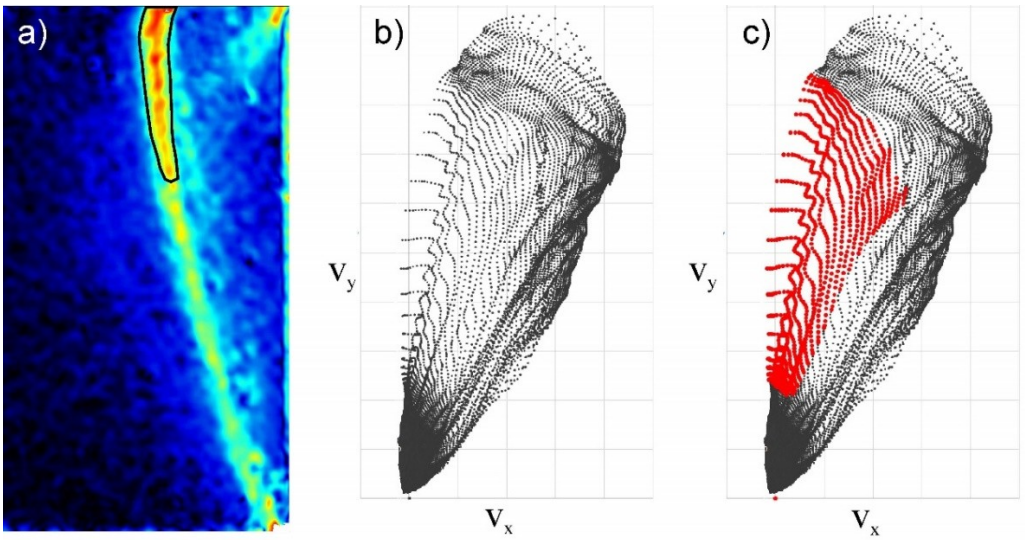

Fig.12. The example of the structure in the experimental data (the final stage of the retaining wall model test: **a)** shear strain map, calculated by DIC, **b)** corresponding scatter plot of the displacement field, **c)** location on the scatter plot of the area circled in black in (a).

4.2. Experimental test

Fig.12 shows the data from the final step of the model test: the shear strain map (a), the original scatter plot (b) and the part of the scatter plot (red dots) corresponding to the area circled in black in (a), superimposed on the complete scatter plot (c). Similar segmentation to that shown in Fig.9 for the DEM simulation appears. The right edge of the red area coincides nicely with one of the lines dividing the original scatter plot into segments, confirming the qualitative similarity between experimental and numerical data.

Based on the preliminary examination presented in this section, we have demonstrated that in the displacement field behind the retaining wall there exists a structure consisting of the strongly constrained near-to-rigid motion zones (DZ), weakly constrained large deformation zones (SZ) and some transition zones (TZ). Material motion in transition zones is quasi-laminar, with the direction of movement constrained and varying displacements. The simple procedure described in Section 4.1 can prove only the existence of the structure in the displacement field. It would be a real challenge to obtain its complete picture, as many time-consuming hand operations are required in this case.

5 *s*-LID analysis

In order to extract the shear zones (SZ) and dead zones (DZ) from the displacement fields in the previous section, it was necessary to calculate the shear strains from the given displacements and perform extensive data filtering.

s-LID analysis, as proposed by Tordesillas et al. (2022) and demonstrated on DEM simulation of an ensemble of spherical grains submitted to planar biaxial compression, offers a better way of investigating structured deformation. To demonstrate this, we will compare the results of the procedure presented in the previous sections with the *s*-LID analysis of the same problem.

5.1. Terminologies used in the s-LID analysis

- Kinematic clusters:
    - clusters found in DSS - grains belong to the same kinematic cluster if they share very similar displacements,
- Kinematic outliers:
    - grains that are moving significantly differently from the others,
    - *s*-LID value, ranging from 0 to +∞, indicates the outlying-ness of a grain's motion - the higher the value, the more outlying the grain's motion is.

The only independent parameter in the *s*-LID analysis is the size of the examined neighbourhood *s*, expressed by the number of belonging measuring points.

5.2 s-LID estimator

The local intrinsic dimensionality LID (Houle, 2017) of the grain motion data in a neighbourhood of the displacement-state space (DSS), centred at the focal grain's displacement, is measured by the *s*-LID estimator, defined by Eq (3):

$$\text{s-LID}(\mathrm{v}) = -\left(\frac{1}{s}\sum_{i=1}^{s}\log\frac{d_i(v)}{d_s(v)}\right)^{-1} \quad , \tag{3}$$

where **v** is the displacement of a focal grain, a 2-dimensional vector representing its translation in the horizontal and vertical directions, $d_i(\mathbf{v})$ is the Euclidean distance between the focal grain displacement and its *i*-th nearest neighbour in DSS; $d_s(\mathbf{v})$ is the maximum of the neighbour distances in DSS; and $s \geq 2$ is a parameter to control the size of the neighbourhood to investigate (i.e., the number of nearest neighbours to use in the estimation procedure). As a result, the *s*-LID is discriminative of the complexity of collective grain motions (Zhou et al., 2021). The results of *s*-LID calculations can be transferred back to the coupled physical space (PSS) to indicate the actual geometric position of areas distinguished by similar *s*-LID values in DSS. Increasing *s* allows the identification of outliers for a larger neighbourhood of DSS, thereby enabling the identification of patterns with more complex kinematics.

5.3 Results of the s-LID analysis for the retaining wall model

Usually, *s*-LID results are given in PSS and DSS space using some colour code. In this paper, the *s*-LID score increases from blue to red - the bluer the colour, the lower the *s*-LID value, indicating no significant difference in the specific grain compared to its nearest neighbours in terms of the motion. Searching for a structure using the *s*-LID estimator requires adopting the neighbourhood size *s*, which may correspond to the searched structure elements (kinematic clusters). The choice of the value depends on the number and density of the measurement points - $s = 25$, for example, corresponds to the area occupied by 5 grains in the case of the

experimental displacement field and 2.5 grains for the DEM simulation. The study of an a priori unknown deformation structure requires selecting the appropriate neighbourhood size and thus applying some range of *s* values by trial and error.

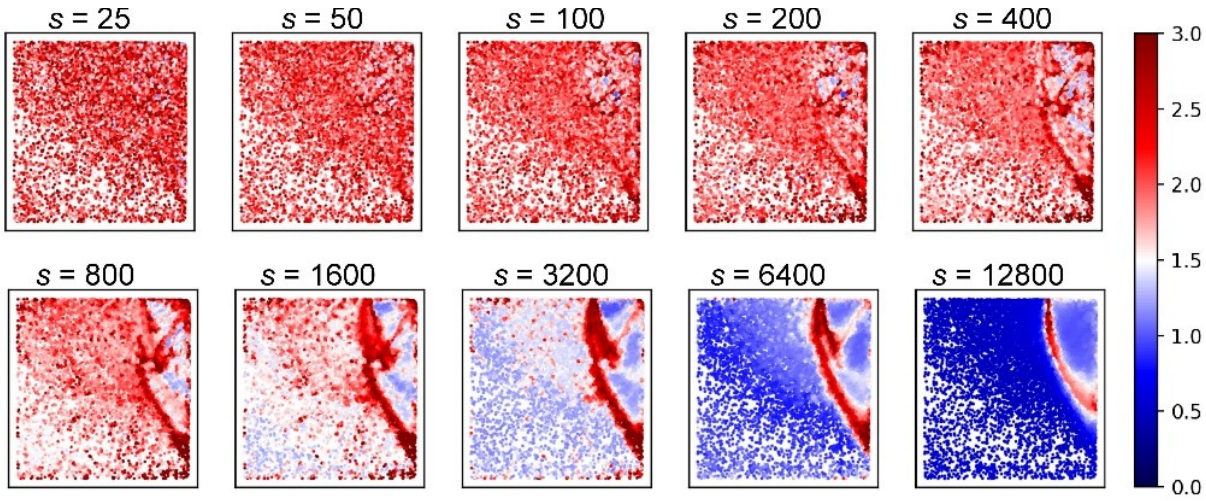

Fig.13. Sensitivity of s-LID analysis results on *s* parameter in PSS space.

Fig.13 gives the results of such a parametric study in PSS space for the selected experimental displacement field and *s* between 25 and 12800. They depend on *s*: up to *s* = 1600, the *s*-LID values uncover a majority of areas with uncoordinated material movement (high *s*-LID score), corresponding mainly to small displacements to the left of the motion wedge but also present inside it.

The explanation of the high s-LID score in the small displacement area (the left side of the *s*-LID maps) is the scale of the selected neighbourhood. From the perspective of 5 grains (s = 25), their small local movements around the equilibrium positions cannot be correlated.

This lack of correlation can result from small, independent local grain movements or a relative error of displacement measurement, which is usually the biggest in the areas of negligible deformation. Despite the relatively high values of *s*-LID in this area, their distribution is random, with no visible structure. Only when the neighbourhood size starts to

compare with some structure elements do the larger scale correlations emerge, as Fig.13 illustrates. It is clear from the figure that there is an optimal value of *s* for the examined displacement field, which reveals the deformation structure most clearly.

Precise determination of this optimal value is quite challenging: the first signs of ordering on the s-LID map appear already for $s = 50$. However, they do not create a continuous structure with dimensions comparable to the model's height. Such a structure appears around $s = 400$ and develops with *s* increasing to around 3200. However, the further increase of *s* causes the structure details to be lost – the tool to look for the structure becomes too big. Instead, the hierarchical order of the various elements can be revealed, e.g. dominant shear band is best isolated at $s = 12800$ (about 2500 grains).

In the next part of the paper, the following values of *s* were selected for further analysis: 400, 600 and 3200 for the DEM simulation and 1600, 3200, 6400 and 12800 for the experimental test. The selected examples of the *s*-LID results for the final step 38 of the DEM simulation are shown in Figs 14, 15b, 16, 17, 21a and 22a. Figs 13, 18, 19 and 20 relate to the experiment. The number of ‘measurement points’ in the original displacement fields had to be down-sampled for *s*-LID analysis to fulfil the software requirements. Due to it the scatter plots presenting *s*-LID results (e.g. Fig.14b) contain less detail than the original ones (e.g. Fig.5f) but preserve enough information to be further studied.

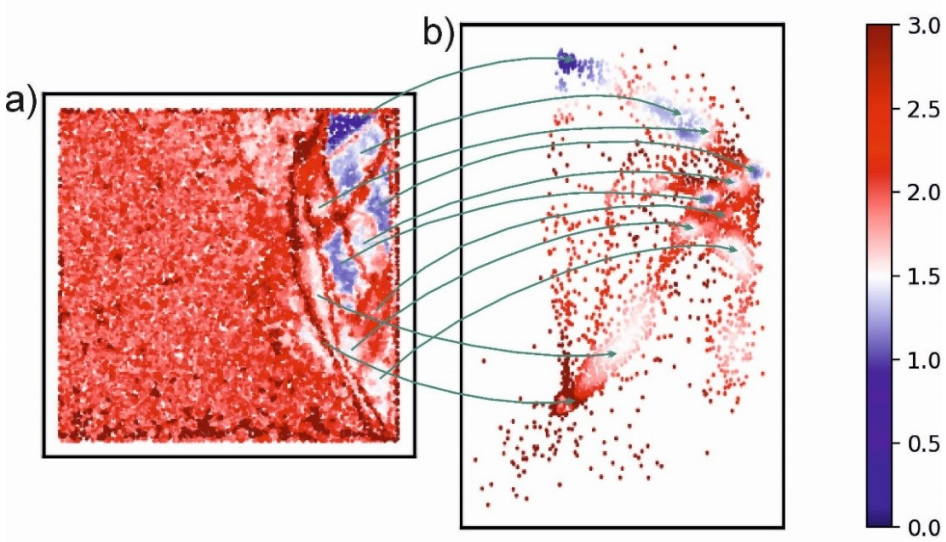

Fig.14. The example of *s*-LID results for DEM simulation of a retaining wall problem (step 38, *s* = 400). Dark blue is attributed to near-rigid motion, dark red - extensive deformation or lack of coordinated motion: **(a)** PSS view, **(b)** corresponding scatter plot (DSS).

This section analyses the *slid_uniform_c* data set, consisting of uniformly down-sampled cumulative displacements. The right side of the map in Fig. 14a shows a network built of intersecting, fine bands with a high *s*-LID score (dark red), suggesting weak bonds between the grains. The areas closed between the bands in the lattice meshes have lower s-LID values, that is, stronger inter-grain bonds, and are marked in Fig.14a with white, pink and shades of blue. The lattice is so well defined that a fairly detailed sketch of it can be made, such as in Figs 15b or 17. Fig.15b shows the sketch of the right part of the network from Fig.14a. It is the region where the corresponding boundary value problem solution using the rigid-plastic approach and the method of characteristics exists.

The typical solution consists of the stress distribution on the top of a retaining wall, determining its bearing capacity and the stress characteristics, forming a so-called 'slip line' field. The slip line field obtained for the retaining wall model used in this paper (both experimental and simulated by DEM) was calculated using the RES program (Leśniewska, 1993). The input data were the geometry of the problem and strength parameters of the granular material: internal friction angle $\hat{\mathfrak{f}} = 30^0$ and soil unit weight $= 16.7 kN/m^3$.

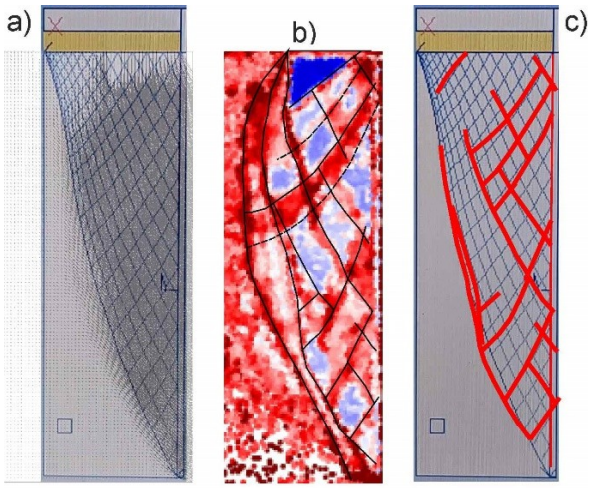

Fig.15. Comparison between the *s*-LID network and the solution of the corresponding boundary value problem using the rigid-plastic approach: **a)** stress characteristics superimposed on the displacement field from Fig.5b, **b)** sketch of the grid of lines dividing the moving wedge area according to the value of the s-LID parameter, **c)** the selected dividing lines with directions close to stress characteristics.

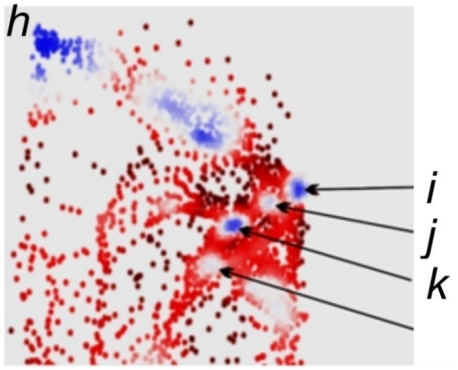

Fig.16. Close-up of Fig.14b – the scatter plot for DEM simulation of a retaining wall problem (step 38, s = 400) – objects ***h*** and ***i*-*k*** recognized in Fig.9c and here.

Fig.15a shows this 'slip line' network superimposed on the displacement field from Fig.5b. The extent of the 'slip line' field coincides nicely with the area of large displacements but not with the region outside it. On the contrary, *s*-LID analysis finds elements of a discrete network also within the area of negligible displacements to the left of the motion area (e.g. Fig.17a).

The sketch of the network consisting of black lines in Fig.15b resembles the solution of a bearing capacity problem for a retaining wall. However, the stress or velocity characteristics represent an un-deformed state, so they do not describe motion and should therefore be

interpreted as indicating its potential and not actual directions. Nevertheless, Fig.15c shows that quite a significant part of the s-LID network (red lines) is close to some directions of the slip line field, which can be the result of the small deformation regime adopted in the experimental program.

The value of *s* (neighbourhood dimension) determines the scale of objects we can extract in the DSS space based on the value of *s*-LID. For example, *s* = 400 finds point-like objects such as those indicated by some green arrows in Fig.14b. The indicated objects have a physical meaning, evidenced by the comparison of their location with the position of the clusters of yellow points in Fig.9c.

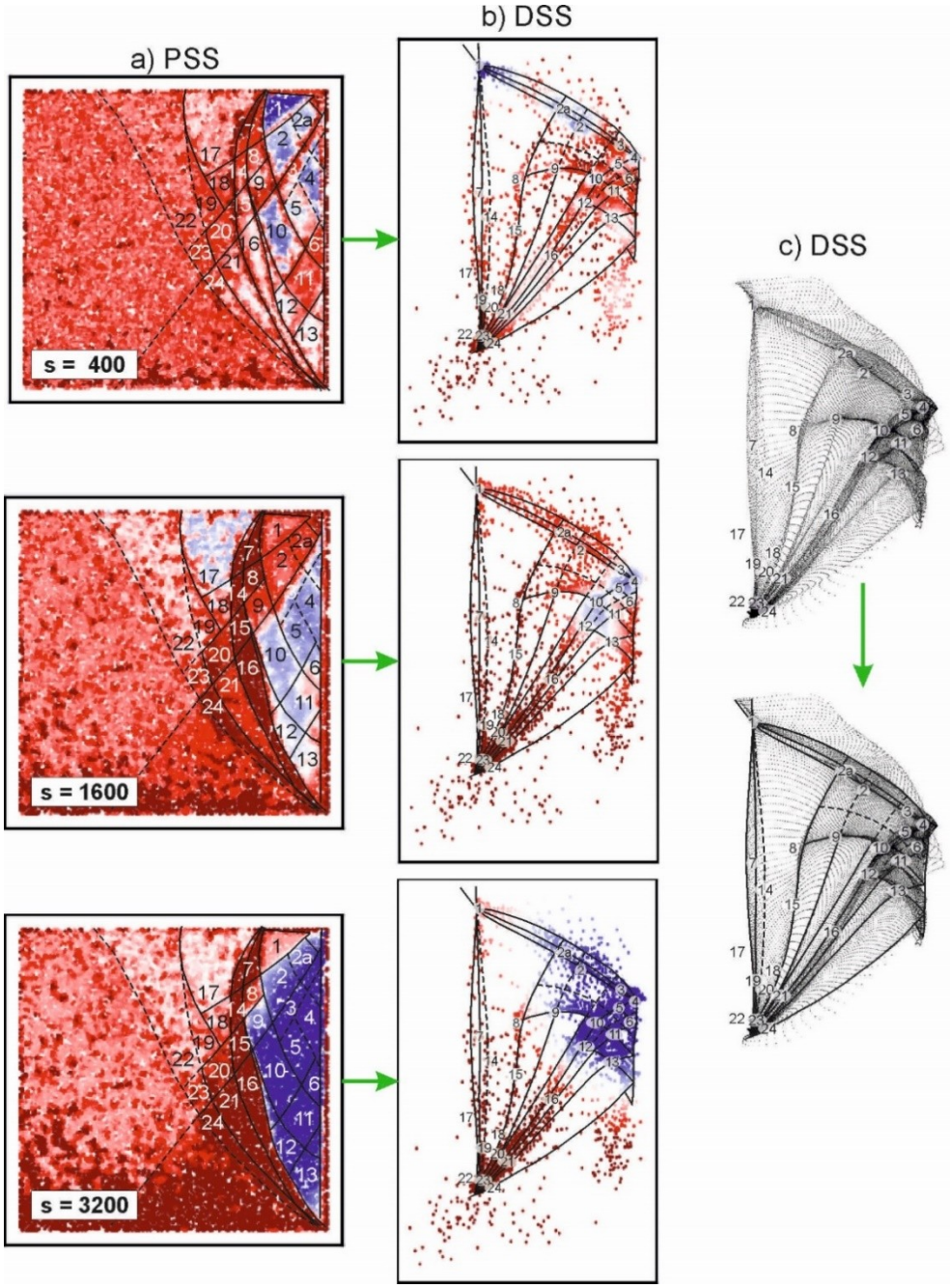

Fig.17. DEM simulation – the study of the influence of the *s* parameter on *s*-LID results.

The same objects can be recognized in both figures, as shown in Fig.16, where the areas marked in Fig.9c as *h*, *i*, *j* and *k* are also present. Fig.17 illustrates the effect of the selected values of *s*. Column a) of this figure shows a sketch of an extended (compared to Fig.15b) grid, delineated on the *s* = 400 map by the high *s*-LID values (black lines) and superimposed on *s* = 1600 and 3200 maps. Each area lying in the meshes of this grid and marked with uniform colour was assigned a number facilitating further analysis.

These areas are approximately diamond-shaped (e.g. 2, 5, 9, 10), triangular (e.g. 1, 4, 6), or take the form of elongated bands (e.g. 3 or 16). They differ significantly in the values of the *s*-LID parameter, which is colour coded according to the scale in Fig.14. For s = 400, the colour of individual meshes differs; within one mesh, it is relatively uniform, suggesting similar kinematics (kinematic cluster).

The dimensions of individual diamond-shaped and triangular clusters are several times smaller than the sample (the height of the model retaining wall). As a result, they can be classified as mesoscale objects at most, except for the bands 7, 14, 15, and 16, whose range covers the entire height of the model, thus classifying them as macro-scale objects. Column b) in Fig.17 shows the results of the *s*-LID analysis of column a) as scatter plots. As these scatter plots include a reduced number of points in the displacement field, for ease of interpretation, a sketch of the division grid of the complete scatter plot is superimposed, marked with solid lines in the lower figure of column c).

Taking advantage of the fact that the area moving as a rigid body in the PSS space corresponds to one point in the DSS space, some clusters in Fig.17 (s = 400) classify as DZ. The point-like objects in DSS (circular objects of relatively small radius) were already pointed out in Fig.16. They are numbered 1, 4, 5 and 10 in Fig.17.

Apart from them, also clusters 2, 2a, 12 and 13 show a tendency to converge around a point in the DSS space. Among the above-mentioned, cluster 1 best meets both conditions for close-to-rigid motion – the lowest *s*-LID score (less than 0.5) and the concentration of the displacement values around one point on the scatter plot. Clusters 4, 5, 10 and 12 show

equally good convergence to a point on the scatter plot, but a higher *s*-LID value, ranging from 0.5 to 1.5.

Changing the size of the neighbourhood from $s = 400$ to $s = 1600$, which is analogous to the change of the magnification in a photograph, i.e. the transition from detailed observation to more coarse but capable of detecting less defined and larger objects, results in merging of some clusters into bigger ones and a new value of their *s*-LID score. The merged clusters still fit into the initial division grid of $s = 400$, in which essential lines do not change, while only some weaker internal ones have disappeared. An example of such a merge is the blue triangle in PSS space, which includes clusters 4-6 and 10-13, forming an object of dimensions in the range of the model's height and uniformly distributed *s*-LID score of about 1.5.

In the DSS space, however, this triangle does not correspond to a circular area concentrated around any point. Instead, it forms a stretched area, filling the characteristic triangle on the right of the scatter plot, the side of which is labelled BB' in Fig.6. For this reason, the large blue triangle in the PSS cannot be considered quasi-rigid. However, since it has been clearly distinguished by the *s*-LID analysis for $s = 1600$, the motion of the points it covers must have some common constraint, revealed in Section 5.4.

Another example of clusters merged in the PSS at $s = 1600$ are 1, 2 and 2a - they gained a similar *s*-LID value around 2.25, and in the DSS space, their displacement points form a part of a well-defined stretched band, limiting the highest displacement values. Due to it, the new cluster cannot classify as DZ. Increasing the value of *s* to 3200 causes a further loss of detail in the PSS and DSS. At the same time, the triangle built in the PSS from areas 3-6 and 10-13 corresponds in the DSS to the above-mentioned well-defined triangle on the right side of the

scatter plot, showing a regular internal division, which proves that the component clusters retain a certain kinematic distinctiveness.

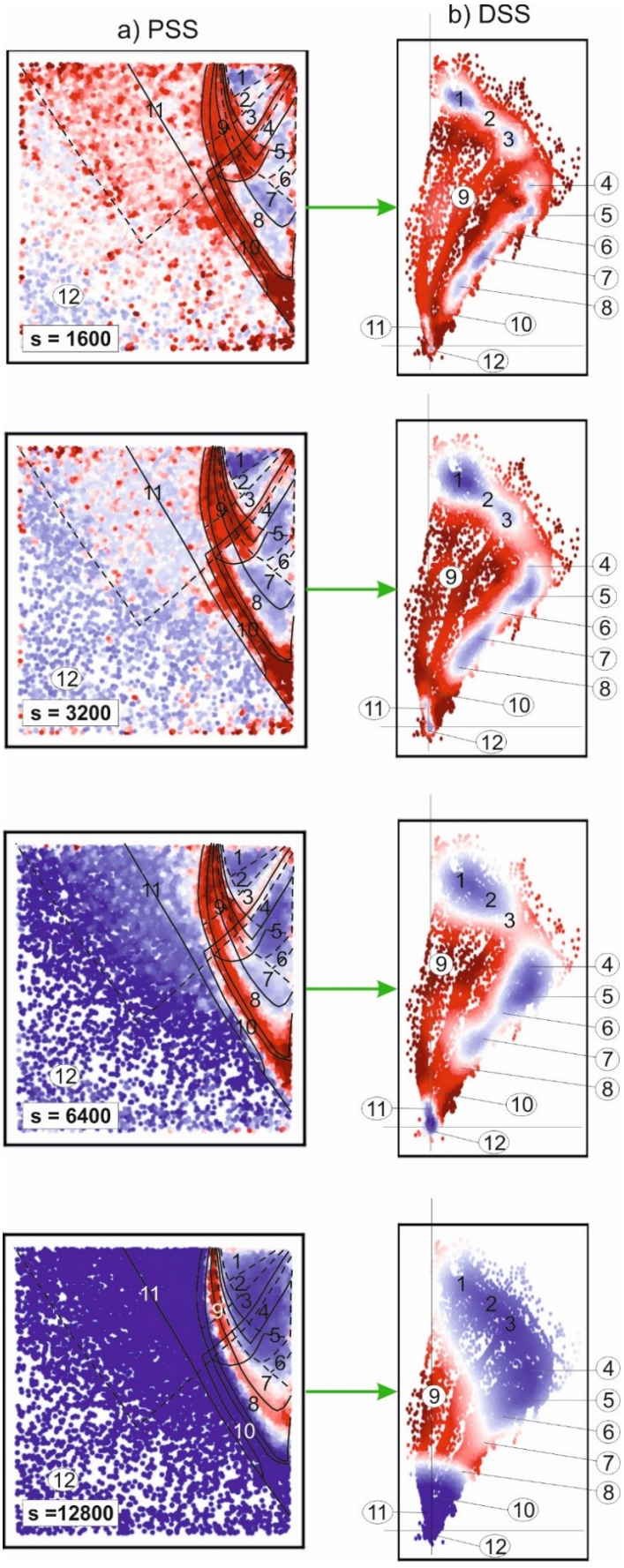

Fig.18. The experimental model test – the study of the influence of the *s* parameter on *s*-LID analysis results.

Clusters 7 and 14-16 belong to the same band, regardless of the size of the *s*. They do not connect with others; the only change is some differences in the values of *s*-LID, ranging from 1.5 to 3.0 (s = 400) and 3.0 or higher (s = 1600 and 3200). Similar observations are made in the analysis of experimental data. Fig.18 shows the example for *s* equal to 1600, 3200, 6400 and 12800.

In the case of s = 1600, cluster 4 is indicated as a quasi-rigid area because its *s*-LID value is relatively low (between 1.0 and 1.5), and its image in the DSS space is a regular circular area of a small radius. The remaining blue clusters (1-3, 5-8) do not satisfy the last condition - their representations in DSS space are quite concentrated but far from a circular shape, suggesting they are kinematically complex. Separating them into components is possible for smaller values of *s*, as evidenced by Fig.19, corresponding to s = 800. A series of circular blue areas of small radii in Fig.19b proves that the small blue clusters visible in Fig.19a classify as DZ.

Further increase of parameter *s* leads to the isolation of the primary shear band, with the highest values of *s*-LID (SZ), which in Fig.18a occurred for s = 12800. It agrees with the previous research on the biaxial test (Tordesillas et al., 2022), where it was found that any persistent shear band is exposed at higher *s* values.

The separation of the primary shear band in the PSS allows its location in the DSS space to be determined. Fig.18b (s = 12800) shows that the localised band of the highest *s*-LID score covers the extended area in the very centre of the scatter plot. A similar location of the primary shear band is also confirmed for the experimental displacement field using the procedure introduced in section 4.1.

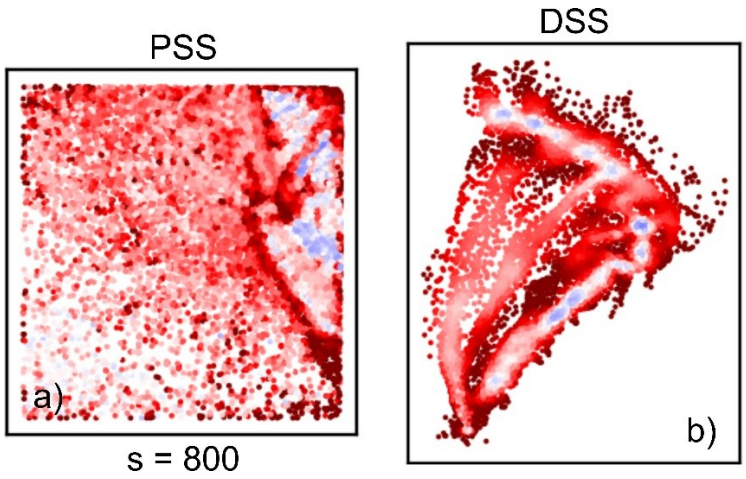

Fig.19. The experimental model test – the result of *s*-LID analysis for *s* = 800.

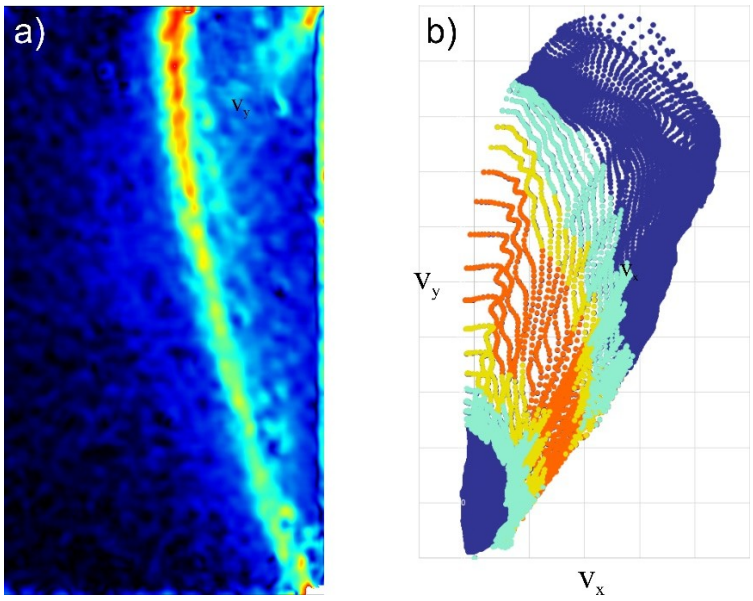

Fig.20. The primary shear band in the experimental model test: PSS **(a)** and DSS space **(b)**.

Fig.20 shows the result - Fig.20a illustrates the shear band in PSS and Fig.20b its transformation on the scatter plot, keeping the colour code from Fig.20a. As can be seen, both figures (18 and 20) locate the primary shear band in the same area of the scatter plot.

It was necessary to calculate shear strains from the displacements to prepare Fig.20. The apparent qualitative agreement between Fig.18 (*s* = 12800) and Fig.20 shows that the *s*-LID analysis is the appropriate independent tool for studying granular materials from a new perspective of local intrinsic dimensionality.

The undoubted advantage of this method, presented in this Section, is its ability not only to reproduce strain localisation from individual grain movements but also to give an insight into the detailed kinematic structure of granular material deformation, inaccessible for the continuum approach.

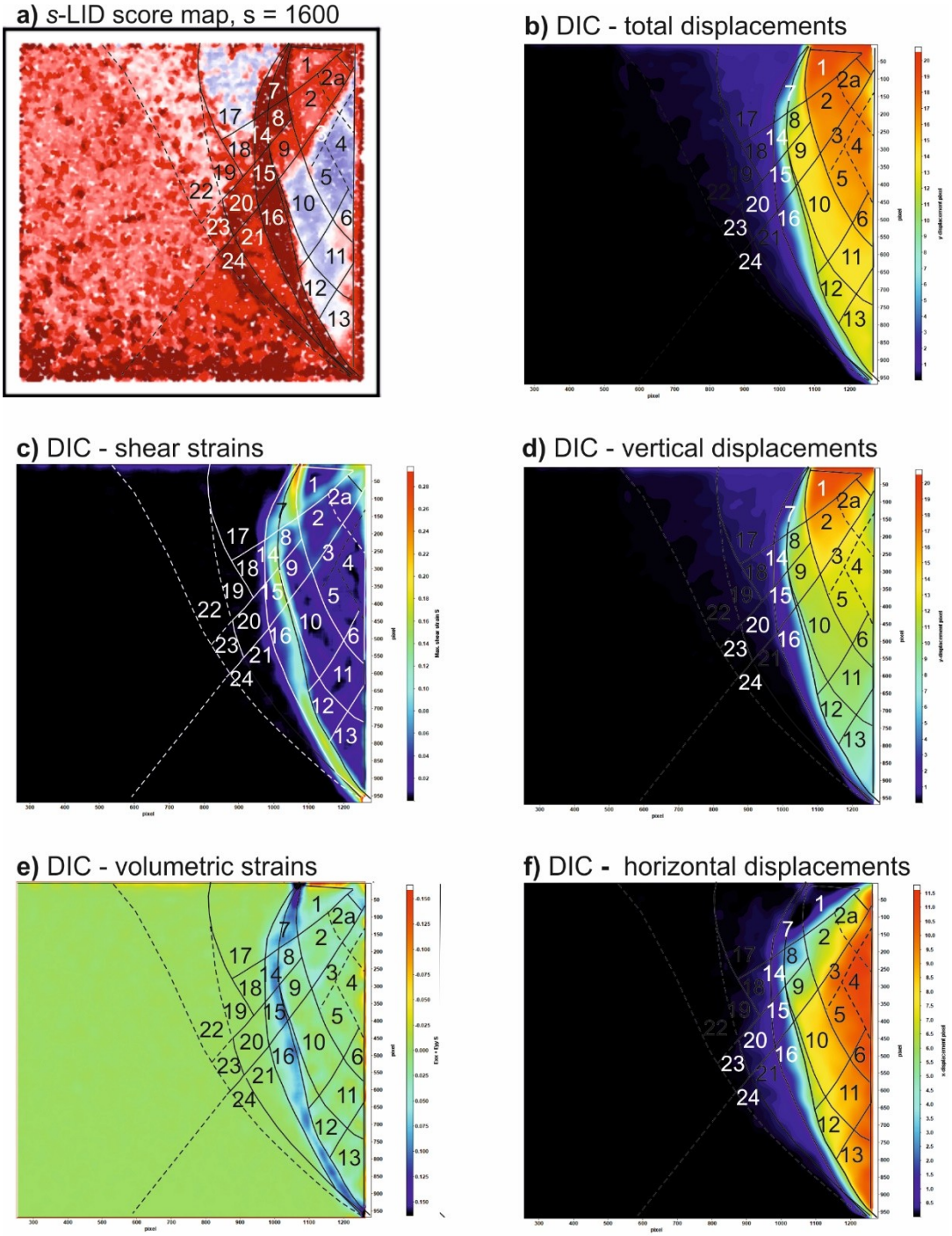

Fig.21. The *s*-LID score map **(a)** versus DIC analysis results **(b)-(f)**.

720

721 *5.4. s-LID and DIC: physical reasons for clusters' forming*

722 To verify *s*-LID results for a retaining wall, the typical results of DIC analysis (maps of
723 displacements and strains), performed for step 38 of the DEM simulation, are compared in
724 Fig.21 with the *s*-LID score map for s = 1600. The same division grid as in Fig.17 is
725 superimposed on the DIC maps.

726

727 The total displacements map (Fig.21b) supplemented by this grid shows the role of the grid's
728 radial lines: they separate the areas of different, uniformly distributed displacement values.
729 The line between clusters 1-7, 2-8, 5-10 and 6-11 coincides with the well-defined border
730 between red (the highest) and yellow (lower) displacement zones. The divisions by the polar
731 lines present in the *s*-LID grid (Fig.21a) are not visible in total displacements but exist in the
732 vertical and horizontal displacement maps (Fig.21d, f).

733

734 The largest vertical displacements concentrate almost exactly in cluster 1, having a relatively
735 high and uniformly distributed *s*-LID score. Clusters 3-6 and 10-13 coincide with the area of
736 most significant horizontal displacements, so it is the displacement direction which makes the
737 common feature connecting them into one entity in Fig.21a (the triangle 3-6, 10-13) and
738 Fig.17 (s = 1600).

739

740 Clusters 1, 2, and 2a move primarily down in a vertical direction, while clusters 2 and 2a, in
741 addition to the predominant downward movement, experience some horizontal displacements,
742 thus constituting the transition zone between the small (cluster 1) and the big (blue) triangle.
743 It follows that the 'polar' lines are associated with a change in the direction of grains'
744 movement.

The clusters above 16 are practically not visible on displacement maps when the full scale of displacements is used, like in Fig.21b, d and f. However, they are visible in Fig.21a, which shows greater sensitivity of the *s*-LID value in the search for kinematic clusters in small displacements region. Such sensitivity gives another essential advantage of the s-LID method - access to areas of small deformation, immeasurable with the DIC method. It may be of great practical importance, e.g., in assessing the risk of landslide movements, which can be very slow in the long initial development period (Zhou et al., 2022).

The maps of shear and volumetric strains (Fig.21c and e) confirm that the highest *s*-LID score, dark red clusters, organized in elongated bands, like 7, 14-16, coincide very well with shear bands and experience significant extension, as expected. Several faint micro shear bands are also present in Fig.21c, inside the high displacement region. They coincide with some of the 'radial' and 'polar' lines detected by *s*-LID analysis in this area. Similar observations are valid for the other steps of the DEM simulation, not shown in this paper. If we narrow the scale in Fig.21e in such a way as to emphasize the volume changes in the area of the wedge between the main shear band and the retaining wall (Fig.22b), numerous clusters subject to slight compression appear. Their location fits well with the *s*-LID partition grid (Fig.22a).

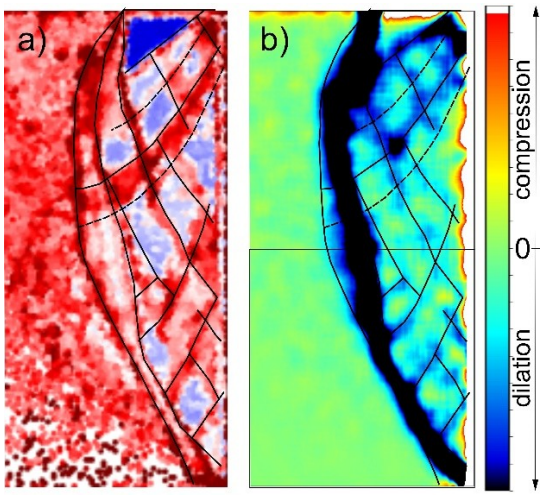

Fig.22. *s*-LID cluster division grid (a) superimposed on volumetric strain map, calculated by DIC (b).

At the same time, the lines of this grid appear to follow the bands of slight extension between the clusters (micro shear bands). It may explain the occurrence of small but stable DZ-s in the area of global deformation behind the retaining wall, the structure of which is determined by the micro shear bands mesh.

6 Summary and conclusions

A recently introduced metric called *s*-LID has been applied to study the classical geotechnical problem of a retaining wall from the perspective of collective motion. A rigid wall translating horizontally out of a granular sample (in active mode) with a constant displacement rate was a specific object of the study.

Granular material movement is usually presented in physical space (PSS). The general advantage of analysing the deformation of granular media in the DSS displacement space is an insight into the processes that are difficult to capture in the PSS, such as forming kinematic clusters with different motion characteristics. Combined with the s-LID method, built on local intrinsic dimensionality, it allows a quantitative assessment of the deformation structure, unavailable with the continuous approach. Several detailed observations come from the study:

- The s-LID method could successfully find shear bands in granular materials without using the concept of continuum strain, thereby making a new independent and powerful tool to study the deformation of granular materials.
- Local intrinsic dimensionality was entirely consistent with the DIC analysis in the areas of significant displacement and expanded the knowledge of the deformation structure in the areas of small displacements, where the DIC method loses its accuracy. This feature may help assess the risk of slow landslide movements.

- The co-existing DZ and SZ constitute the deformation structure behind a retaining wall. They differ in scale: SZ have prevailing dimensions in the range of the model height and DZ are more numerous but much smaller, having two comparable dimensions determined by the meshes of the *s*-LID dividing grid, where they occur.
- It is easy to recognize near-to-rigid zones (DZ) in DSS, even in the area of high displacements, by their point-like representations and low s-LID score.
- SZ can be kinematically complex – the primary shear band, in the case of the studied retaining wall problem, exhibited internal structure and consisted of several segments of different types of motion,
- results of the *s*-LID analysis are *s* sensitive - the study of an a priori unknown deformation structure requires selecting the appropriate neighbourhood size and thus applying some range of *s* values by trial and error.

Acknowledgements

This research was funded in part by National Science Centre, Poland, grant no. 2020/39/B/ST8/01685. For the purpose of Open Access, the authors have applied a CC-BY public copyright licence to any Author Accepted Manuscript (AAM) version arising from this submission.

Bibliography

Coulomb, C.A. (1776) Essai sur une application des regles de maximis et minimis a quelqes problemas de stratique relatifs a l'architecture. Memoires de mathematique et de physique. Presentes a l'Academie Royale des Sciences, pp. 343–382.

Chèvremont W., Bodiguel H., Chareyre B. (2020) Lubricated contact model for numerical simulations of suspensions. Powder Technology (372), 600 - 610. DOI: doi.org/10.1016/j.powtec.2020.06.001

Cui, D., Wu, W., Xiang, W., Doanh, T., Chen, Q., Wang, S., Liu, Q., Wang, J. (2017) Stick–slip behaviours of dry glass beads in triaxial compression. Granul. Matter 19(1), 111.

Fathipour, H., Payan, M., Chenari, RJ, Senetakis, K. (2021) Lower bound analysis of modified pseudo-dynamic lateral earth pressures for retaining wall-backfill system with depth-varying damping using FEM-Second order cone programming, Int J Numer Anal Methods Geomech. 45:2371–2387.

Franks, D. M., Stringer, M., Torres-Cruz L.A., Baker E., Valenta R., Thygesen, K., Matthews, A., Howchin J. & Barrie, S. (2021) Tailings facility disclosures reveal stability risks, Nature Scientific Reports 11:5353, https://doi.org/10.1038/s41598-021-84897-0

Frost J.D., Dejong J.T., Recalde M. (2002). Shear failure behavior of granular-continuum interfaces. Eng Fract Mech 69(17):2029–2048

Greco, V. (2013). Active Thrust on Retaining walls of Narrow Backfill Width. Comput. Geotechnics 50, 66–78. doi:10.1016/j.compgeo.2012.12.007

Gu X., Chen Y., Huang M. (2017) Critical state shear behavior of the soil-structure interface determined by discrete element modeling. Particuology 35:68–77

Guan, X., Madabhushi, G.S.P. (2022), Dynamic response of a retaining wall with a structure on the dry backfill, Soil Dynamics and Earthquake Engineering 157, 107259, //doi.org/10.1016/j.soildyn.2022.107259

Hall, S.A., Muir Wood, D., Ibraim, E., Viggiani, G.(2010) Localised deformation patterning in 2D granular materials revealed by digital image correlation, Granular Matter 12:1–14 doi: 10.1007/s10035-009-0155-1.

Hartmann P., Thoeni K., Rojek J. (2022) A generalised multi-scale peridynamics – DEM framework and its application to rigid–soft particle mixtures. Computational Mechanics, DOI: 10.1007/s00466-022-02227-1

Hegde, A., Murthy, T.G. (2022) Experimental studies on deformation of granular materials during orthogonal cutting. Granular Matter 24, 70.

Hossein, K. M., Hassan, S., Thirapong, P., Araz, S. (2022) Active Earth Pressure Distribution inside Narrow Backfill Considering Soil-Arching Effect, International Journal of Geomechanics, Vol 22, No 7, doi: 10.1061/(ASCE) GM.1943-5622.0002434.

Houle, M.E.(2017) Local intrinsic dimensionality i: an extreme-value-theoretic foundation for similarity applications. In: SISAP, pp. 64–79.

Houle, M.E. (2017) Local intrinsic dimensionality ii: multivariate analysis and distributional support. In: SISAP, pp. 80–95.

Hu, W., Zhu, X., Zeng, Y. et al. (2022) Active earth pressure against flexible retaining wall for finite soils under the drum deformation mode. Sci Rep 12, 497, https://doi.org/10.1038/s41598-021-04411-4

James, R.G. (1965) Stress and strain fields in sand, PhD Thesis, University of Cambridge.

James, R. G. and Bransby, P. L. (1971) A velocity field for some passive earth pressure problems. Geotechnique21, 61–83.

Ke, W., Luo, W., Fang, T., Chen, Q., Xu, Ch., Yan, J. (2020) A simple closed-form solution for kinematic responses of retaining wall incorporating the effects of shear stiffness of soils, Soil Dynamics and Earthquake Engineering 134, 106163, //doi.org/10.1016/j.soildyn.2020.106163

Khosravi, MH, Pipatpongsa, T., Takemura, J. (2016) Theoretical analysis of earth pressure against rigid retaining walls under translation mode, Soils and Foundations 56(4):664–675, //dx.doi.org/10.1016/j.sandf.2016.07.007

Khosravi, MH, Sarfaraz, H., Pipatpongsa, T. and Sharifdeljuyi, A., (2022) Active Earth Pressure Distribution inside Narrow Backfill Considering Soil-Arching Effect, https://doi.org/10.1061/(ASCE)GM.1943-5622.0002434

Kozicki, J., Donze, F.V. (2008) A new open-source software developer for numerical simulations using discrete modelling methods. Comput. Methods Appl. Mech. Eng. 197, 4429–4443.

Kozicki J., Gladky A., Thoeni K. (2022) Implementation of high-precision computation capabilities into the open-source dynamic simulation framework YADE. Computer Physics Communications, DOI: 10.1016/j.cpc.2021.108167

Kozicki, J., Niedostatkiewicz, M., Tejchman, J., Mühlhaus, H.-B. (2013) Discrete modelling results of a direct shear test for granular materials versus FE results. Granul. Matter 15(5), 607–627.

Lai F., Yang D., Liu S., Zhang H., Cheng Y.(2022) Towards an improved analytical framework to estimate active earth pressure in narrow c – ϕ soils behind rotating walls about the base, Computers and Geotechnics, 141.

Leśniewska, D (1993), RES — A numerical program for reinforced-soil slopes based on the rigid-plastic theoretical model, Geotextiles and Geomembranes, 12, 5, 435-439, DOI: 10.1016/0266-1144(93)90018-J

Leśniewska, D. & Muir Wood, D. (2009). Observations of stresses and strains in a granular material. J Engng Mech., ASCE 135,No. 9, 1038–1054, doi: 10.1061/_ASCE_EM.1943-7889.0000015.

Leśniewska, D. (2000) Shear Band Pattern Formation in Soil. Monograph, Institute of Hydro-Engineering, Polish Academy of Science, Gdańsk, Poland, doi:10.13140/2.1.3653.0244.

Leśniewska, D. &Mróz, Z. (2000). Geotechnique 50, No. 5, 521-536,

Leśniewska, D. and Muir Wood, D. (2010) Photoelastic and photographic study of a granular material. Geotechnique 60, 903–911, doi: 10.1680/geot.2010.60.00.1.

Leśniewska, D., Nitka,· M., Tejchman, J., Pietrzak, M., 2020, Contact force network evolution in active earth pressure state of granular materials: photo-elastic tests and DEM, Ganular Matter (2020) 22:71, https://doi.org/10.1007/s10035-020-01033-x.

Loukidis D., Salgado R. (2013) Active earth thrust on walls supporting granular soils: effect of wall movement, Proceedings of the 18th International Conference on Soil Mechanics and Geotechnical Engineering, Paris 2013, 2043-2046

Luding S. (2004) Micro-macro transition for anisotropic, frictional granular packings. Int. J. Solids Struct., 41:5821-5836

McGovern, D.J., Allsop, W., Rossetto, T., Chandler, I. (2023) Large-scale experiments on tsunami inundation and overtopping forces at vertical sea walls, Coastal Engineering 179, doi.org/10.1016/j.coastaleng.2022.104222

Milligan, G.W.E. (1974a). The Behaviour of Rigid and Flexible Retaining Walls in Sand, PhD Thesis, University of Cambridge .

Milligan, G. W. E. (1974b). The behaviour of rigid and flexible retaining walls in sand. Geotechnique 26, 473–494.

Milligan, G. W. E. (1983) Soil deformations near anchored sheet-pile walls. Geotechnique 33, 41–55.

Maurin R. (2018) YADE 1D vertical VANS fluid resolution : validations. Yade Technical Archive.

Muir Wood, D. and Leśniewska, D. (2011) Stresses in granular materials. Granular Matter 13, 395–415, doi: 10.1007/s10035-010-0237-0.

Nitka M., Grabowski A. (2021) Shear band evolution phenomena in direct shear test modelled with DEM. Powder Technology, 391:369-384

Rechenmacher, A. L. and Finno, R. J. (2004) Digital image correlation to evaluate shear banding in dilative sands. Geotechnical Testing Journal, 27, 13-22

Ren, F., Huang, Q., Chen, J. (2022) Centrifuge modelling of geosynthetic-reinforced soil retaining walls subjected to the combined effect of earthquakes and rainfall, Geotextiles and Geomembranes 50, 470–479

Sailer, E., Taborda, DMG, Zdravkovi´c, L., Potts, DM, Cui, W. (2021) Thermo-hydro-mechanical interactions in porous media: Implications on thermo-active retaining walls, Computers and Geotechnics 135, 104121, https://doi.org/10.1016/j.compgeo.2021.104121

Salazar A., Sáez E., Pardo G. (2015) Modeling the direct shear test of a coarse sand using the 3D discrete element method with a rolling friction model. Comput. Geotech., 67:83-93

Schmüdderich, C., Tschuchnigg, F. &Schweiger, H.F. (2022) Significance of flow rule for the passive earth pressure problem. ActaGeotech. 17, 81–92.

Schmüdderich, C., Tschuchnigg, F.,Wichtmann T.(2020) Rigorous lower and upper bounds for the 3D passive earth pressure problem, Géotechnique Letters, Volume 10 Issue 2, pp. 100-105, June.

Slominski, C. C., Niedostatkiewicz, M. and Tejchman, J. (2007) Application of particle image velocimetry (PIV) for deformation measurement during granular silo flow. Powder Technology, 173, 1-18

Stanier, S., Dijkstra, J., Lesniewska, D., Hambleton, J., White, D., Muir Wood, D., (2016) Vermiculate artefacts in image analysis of granular materials. Computers and Geotechnics 72, 100-113, DOI: 10.1016/j.compgeo.2015.11.013

Schweiger H. F., Tschuchnigg F.(2021) A numerical study on undrained passive earth pressure, Computers and Geotechnics, 140.

Thoeni, K., Giacomini, A., Lambert, C., Sloan, S.W., Carter, J.P. (2014) A 3Ddiscrete element modelling approach for rockfall analysis with drapery systems. International Journal of Rock Mechanics and Mining Sciences 68, 107119, DOI:10.1016/j.ijrmms.2014.02.008.

Thoeni K. (2021) A novel and robust contact detection algorithm for arbitrarily shaped blocks. Computers and Geotechnics, DOI: 10.1016/j.compgeo.2021.104430

Tordesillas, A., Zhou, S., Bailey, J. and Bondell, H. (2022) A representation learning framework for detection and characterization of dead versus strain localization zones from pre- to post- failure, Granular Matter.

Wang K, Liu G, Zhang Y and Lin J (2022) Quantification of the Active Lateral Earth Pressure Changes on Retaining Walls at the Leading Edge of Steep Slopes. *Front. Earth Sci.* 10:796232.

White, D. J., Take, W. A. and Bolton, M.D. (2003) Soil deformation measurements using particle image velocimetry (PIV) and photogrammetry. Geotechnique 53, 619-631.

White, D. J., Randolph, M. and Thompson, B. (2005) An image based deformation measurement system for the geotechnical centrifuge., Int. Jnl Phys. Model. Geotech. 3, 1-12

Widulinski, L., Tejchman, J., Kozicki, J., Leśniewska, D. (2011) Discrete simulations of shear zone patterning in sand in earth pressure problems of a retaining wall. Int. J. Solids Struct. 48(7–8), 1191–1209.

Xu, L., Xu Y., Wang, C. and Feng, K. (2019) Data-Driven Deformation Reliability of Retaining Structures in Deep Excavations Considering Measurement Error Appl. Sci. 2019, 9, 5466; doi:10.3390/app9245466.

Xua, P., Hatamib, K., Baoc, JJ., Lid T. (2020) Bearing capacity and failure mechanisms of two-tiered reinforced soil retaining walls under footing load, Computers and Geotechnics 128, 103833

Yang, M. and Deng, B. (2019). Simplified Method for Calculating the Active Earth Pressure on Retaining Walls of Narrow Backfill Width Based on DEM Analysis. Adv. Civil Eng. 2019, 1–12. doi:10.1155/2019/1507825

Yang, Z., Liu, J., Nie J., Li X. (2022) Efficient estimation of cumulative distribution functions of multiple failure modes using advanced generalized subset simulation, Int J Numer Anal Methods Geomech. 2022;46:1093–1108.

Zhao S., Evans T.M., Zhou X. (2018) Shear-induced anisotropy of granular materials with rolling resistance and particle shape effects. Int. J. Solids Struct., 150 (1):268-281

Zhou, S., Tordesillas, A., Pouragha, M., Bailey, J., Bondell, H. (2021) On local intrinsic dimensionality of deformation in complex materials. Sci. Rep. 11(1), 1

Zhou, S., Tordesillas, A., Intrieri, E., Di Traglia, F., Qian, G., & Catani, F. (2022). Pinpointing early signs of impending slope failures from space. Journal of Geophysical Research: Solid Earth, 127, e2021JB022957. https://doi. org/10.1029/2021JB022957

List of symbols and abbreviations

PSS - the physical state space, where the measurement points (e.g. grains) are described in 2D (x, y) space by their x and y coordinates

v_x, v_y - the horizontal and vertical displacements

v_z - the out-of-plane displacement

DSS - the displacement state space, where the measurement points (e.g. grains) are described in 2D (v_x, v_y) space by horizontal and vertical displacements

LID - the local intrinsic dimensionality

s - a number of the nearest neighbours in DSS (the size of the investigated neighbourhood)

*s*NN - *s* nearest neighbours (grains)

s-LID - the measure quantifying how outlying a grain's motion is relative to its *s* nearest neighbours in DSS

DEM - discrete element method

DIC - discrete image correlation

P-3D test - pseudo three-dimensional test

E_c - modulus of elasticity of grain contact

ν_c - Poisson ratio of the grain contact

φ - inter-particle friction angle

- coefficient of rolling stiffness

- rolling coefficient

R - particle (grain) radius

ρ - particle density

a - numerical damping parameter

DZ - ‘dead’ zone – quasi rigid cluster

SZ - shear zone

TZ - transition zone

D_{50}- median particle diameter

d_k- total displacement of a focal measuring point after k time steps

$d_{N\text{-}av}$- mean displacement of the neighbourhood consisting of N measuring points

$^{\circ}\mathbf{v}$ - the difference between the selected focal point displacement and the average displacement of its neighbourhood

v - the focal grain displacement vector

$d_i(\mathbf{v})$ - the Euclidean distance between the focal grain displacement and its i-th nearest neighbour in DSS

$d_s(\mathbf{v})$ - maximum of the neighbour distances in DSS

949

950 **Tables**

951

952 **Table 1:** Material constants used in DEM simulations

E_c [GPa]	ν_c [-]	μ [$^\circ$]	β [-]	η [-]	R [m]	ρ [kg/m^3]	α [-]
2.4	0.3	20	0.3	0.005	0.001	2550	0.08

953

Figures' captions:

Fig.1. Radiographs made at Cambridge University, showing examples of soil failure patterns (*structured deformation*) behind flexible (a) and rigid (b) model retaining walls. White dots on the radiographs are images of lead shot markers.

Fig.2. The out-of-plane grain displacement v_z in 3D DEM simulation of a P-3D test. a) schematic geometry of a sample in a P-3D test, b), c), d) – v_z as a function of z, y and x.

Fig.3. Idealized case - a rigid wedge sliding on an inclined plane: a) discretized displacement field, b) scatter plot, c) evolution of the wedge displacement as a function of the number of wall displacement increments (time steps).

Fig.4. The layout of the retaining wall model test and its boundary conditions: the incremental horizontal translation of the right boundary and constant external loading of the top boundary (through five adjusting rigid blocks, Leśniewska et al., 2020).

Fig.5. Displacement data, representing the initial stage of the experiment (left column) and the final stage of the DEM simulation (right column): **(a)**, **(b)** - displacement vectors, **(c)**, **(d)** - the corresponding shear strain maps (PSS), **(e)**, **(f)** - displacement fields (a) and (b) as scatter plots (DSS).

Fig.6. Approximate division of the scatter plots, representing: **a)** the initial stage of the experiment (Fig.5e), **b)** the final stage of the DEM simulation (Fig.5f).

Fig.7. Scatter plots of displacements after steps 01, 08, 18, 28 and 38 of the DEM simulation.

Fig.8. Areas of different shear strain values selected for data interpretation in DSS: **a)** – the approximate location on the shear strain map, **b)** – extension and colour code.

Fig.9. Scatter plots with the reduced number of points showing locations corresponding to the areas from Fig.8b in DSS space.

Fig.10. Displacement value evolution for the selected focal points compared to their closest neighbourhood's average displacement in the areas: **a)** *a*, *e* and *c*, **b)** *b* and *d*, **c)** *h*, *i* and *n* (Fig.8b).

Fig.11. The statistical trend of the difference between the selected focal points' displacements and the average displacement of their neighbourhoods, in areas **a**, **d** and **h** in Fig.8b.

Fig.12. The example of the structure in the experimental data (the final stage of the retaining wall model test: **a)** shear strain map, calculated by DIC, **b)** corresponding scatter plot of the displacement field, **c)** location on the scatter plot of the area circled in black in (a).

Fig.13. Sensitivity of s-LID analysis results on *s* parameter in PSS space.

Fig.14. The example of *s*-LID results for DEM simulation of a retaining wall problem (step 38, $s = 400$). Dark blue is attributed to near-rigid motion, dark red - extensive deformation or lack of coordinated motion: **(a)** PSS view, **(b)** corresponding scatter plot (DSS).

Fig.15. Comparison between the *s*-LID network and the solution of the corresponding boundary value problem using the rigid-plastic approach: **a)** stress characteristics superimposed on the displacement field from Fig.5b, **b)** sketch of the grid of lines dividing the moving wedge area according to the value of the s-LID parameter, **c)** the selected dividing lines with directions close to stress characteristics.

Fig.16. Close-up of Fig.14b – the scatter plot for DEM simulation of a retaining wall problem (step 38, $s = 400$) – objects ***h*** and ***i*-*k*** recognized in Fig.9c and here.

Fig.17. DEM simulation – the study of the influence of the *s* parameter on *s*-LID results.

Fig.18. The experimental model test – the study of the influence of the *s* parameter on *s*-LID analysis results.

Fig.19. The experimental model test – the result of *s*-LID analysis for *s* = 800.

Fig.20. The primary shear band in the experimental model test: PSS **(a)** and DSS space **(b)**.

Fig.21. The *s*-LID score map **(a)** versus DIC analysis results **(b)**-**(f)**.

Fig.22. *s*-LID cluster division grid (a) superimposed on volumetric strain map, calculated by DIC (b).